HAL
open science

Systematic effects on the size–luminosity relations of early- and late-type galaxies: dependence on model fitting and morphology

M. Bernardi, A. Meert, V. Vikram, M. Huertas-Company, S. Mei, F. Shankar, R. Sheth

▶ **To cite this version:**

M. Bernardi, A. Meert, V. Vikram, M. Huertas-Company, S. Mei, et al.. Systematic effects on the size–luminosity relations of early- and late-type galaxies: dependence on model fitting and morphology. Monthly Notices of the Royal Astronomical Society, 2014, 443 (1), pp.874-897. 10.1093/mnras/stu1106 . hal-02547664

HAL Id: hal-02547664

https://hal.science/hal-02547664v1

Submitted on 8 Dec 2023

HAL is a multi-disciplinary open access archive for the deposit and dissemination of scientific research documents, whether they are published or not. The documents may come from teaching and research institutions in France or abroad, or from public or private research centers.

L'archive ouverte pluridisciplinaire **HAL**, est destinée au dépôt et à la diffusion de documents scientifiques de niveau recherche, publiés ou non, émanant des établissements d'enseignement et de recherche français ou étrangers, des laboratoires publics ou privés.

Monthly Notices of the ROYAL ASTRONOMICAL SOCIETY

MNRAS **443,** 874–897 (2014) doi:10.1093/mnras/stu1106

Systematic effects on the size–luminosity relations of early- and late-type galaxies: dependence on model fitting and morphology

M. Bernardi,[1★] A. Meert,[1] V. Vikram,[1] M. Huertas-Company,[2] S. Mei,[2] F. Shankar[2] and R. K. Sheth[1,3]

[1]*Department of Physics and Astronomy, University of Pennsylvania, Philadelphia, PA 19104, USA*
[2]*GEPI, Observatoire de Paris, CNRS, Univ. Paris Diderot 5 Place Jules Janssen, F-92190 Meudon, France*
[3]*The Abdus Salam International Centre for Theoretical Physics, Strada Costiera 11, I-34151 Trieste, Italy*

Accepted 2014 June 2. Received 2014 June 2; in original form 2012 November 26

ABSTRACT

We quantify the systematics in the size–luminosity relation of galaxies in the Sloan Digital Sky Survey main sample (i.e. at $z \sim 0.1$) which arise from fitting different one- and two-component model profiles to the r-band images. For objects brighter than L_*, fitting a single Sérsic profile to what is really a two-component SerExp system leads to biases: the half-light radius is increasingly overestimated as n of the fitted single component increases; it is also overestimated at $B/T \sim 0.6$. For such objects, the assumption of a single Sérsic component is particularly misleading. However, the net effect on the $R-L$ relation is small, except for the most luminous tail. We then study how this relation depends on morphology. Our analysis is one of the first to use Bayesian-classifier-derived weights, rather than hard cuts, to define morphology. For the $R-L$ relation Es, S0s and Sas are early types, whereas Sbs and Scds are late, although S0s tend to be 15 per cent smaller than Es of the same luminosity, and faint Sbs are more than 25 per cent smaller than faint Scds. Neither the early- nor the late-type relations are pure power laws: both show significant curvature, which we quantify. This curvature confirms that two mass scales are special for both early- and late-type galaxies: $M_* \sim 3 \times 10^{10}$ and $2 \times 10^{11}\,\mathrm{M}_\odot$. Also, although the $R_{\rm disc}-L_{\rm disc}$ and $R_{\rm disc}-M_{*\rm disc}$ relations of discs of disc-dominated galaxies run parallel to the corresponding relations for the total light in late types (i.e. they are significantly curved), $R_{\rm bulge}-L_{\rm bulge}$ and $R_{\rm bulge}-M_{*\rm bulge}$ for bulge-dominated systems show almost no curvature (i.e. unlike for the total light of early-type galaxies). Finally, the intrinsic scatter in the $R-L$ relation decreases at large L and/or M_* and should provide additional constraints on models of how the most massive galaxies formed.

Key words: galaxies: bulges – galaxies: elliptical and lenticular, cD – galaxies: evolution – galaxies: fundamental parameters – galaxies: photometry.

1 INTRODUCTION

The spatial (and colour) distribution of star light in a galaxy is thought to encode information about its formation history, so there has been considerable interest in developing accurate descriptions of the projected surface brightness distribution of galaxies.

One approach to this problem is to fit the free parameters of a predetermined functional form to the observed surface brightness profile. These derived free parameters (typically, these are expressed in terms of the scale which contains half the total light, and the surface brightness at this scale) are more useful if the functional form itself actually does provide a good fit to the profile. A simple version of this approach is to fit many different functional forms to the data, and then select the one which provides the best fit (in some suitably quantified way). For example, the Sloan Digital Sky Survey (SDSS; Stoughton et al. 2002) reports fits of both exponential ($I(\theta) \propto \exp(-\theta/\theta_1)$) and de Vaucouleurs ($\propto \exp[-(\theta/\theta_4)^{1/4}]$) profiles to the image, along with an estimate of which fits better.

The exponential and de Vaucouleurs (1948) profiles are special cases ($n = 1$ and 4) of the Sérsic (1968) profile

$$I(\theta) = I_n \exp[-(\theta/\theta_n)^{1/n}]. \quad (1)$$

With sufficiently good data, it is possible to simply fit a Sérsic profile to the data, leaving the fitting procedure to determine n as well as I_n and θ_n. If galaxies really are intrinsically single Sérsics with a wide range of n, then the parameters (e.g. half-light radius) returned by forcing $n = 1$ or 4 in the single component fits will generally be biased. Across the population as a whole, the derived value of n spans a wide range, sometimes being as large as ∼8 or

★E-mail: bernardm@sas.upenn.edu

© 2014 The Authors
Published by Oxford University Press on behalf of the Royal Astronomical Society

Downloaded from https://academic.oup.com/mnras/article/443/1/874/1471537 by guest on 08 December 2023

10 (e.g. Simard et al. 2011, and references therein), suggesting that forcing $n = 1$ or 4 is ill advised.

Of course, it is not obvious that the light profile should be fitted using a single component. The stellar kinematics in many galaxies indicate that the stars define more than one dynamical component. Examples include counter-rotating discs, as well as disc systems with bulges or bars in their centres (e.g. Emsellem et al. 2011). Evidence for more than one component is often seen in the chemical composition as well (e.g. Johnston et al. 2012). In such galaxies, it is interesting to see if the light profile also indicates the presence of more than one component.

This has motivated studies which model the observed profile as the sum of an exponential and a de Vaucouleurs profile; what we will call the deVExp model. (Of course, since there are now more free parameters to be fit, better, higher resolution data are required. In this context, it is worth noting that Sérsics initial motivation was to fit a functional form with fewer free parameters which would allow one to interpolate between two-component systems having varying fractions of an $n = 4$ bulge and an $n = 1$ disc.) It is common to report the result of such two-component fits in terms of the fraction of the total light that is in the bulge (de Vaucouleurs) component: B/T. Correlations of these B/T values with other parameters (e.g. luminosity) are then used to constrain formation history scenarios.

On the other hand, if galaxies really are single component Sérsics, and one attempts to fit them with two-component deVExp profiles, then one will infer an entirely spurious B/T value (the profile was, after all, just a single component). This spurious B/T will correlate with other parameters if n itself does, complicating the interpretation of such correlations. Indeed, some have argued that the evidence for two components in the light profile is sometimes just a consequence of trying to fit what is really a single component Sérsic with a linear combination of exponential and de Vaucouleurs profiles (e.g. Graham et al. 2003), although this leaves unanswered the question of why dynamically or chemically distinct components do not leave a signature in the light.

In recent years, the correlation between size and luminosity for early-type galaxies has received much attention, because high redshift early types appear to be more compact than their counterparts at low redshift (e.g. Trujillo et al. 2006; Cimatti et al. 2008; van Dokkum et al. 2008; Bruce et al. 2012). However, both the size and the luminosity estimates, R and L, are derived parameters, obtained by fitting to the observed surface brightness distribution. As a result, they depend on assumptions about the intrinsic shape of the surface brightness profile. For example, if the fit assumes that galaxies are made up of two components or just one, and if two, whether they are modelled as the sum of an exponential and a de Vaucouleurs (1948) profile, an exponential and a Sérsic (1968), or two Sérsics.

The main goal of this paper is to quantify the systematics on the local R–L relation which are associated with the choice of a particular model. In practice, 'local' means the 5×10^5 galaxies at $z \sim 0.1$ in Seventh Data Release (DR7) of the SDSS Main Galaxy sample (Abazajian et al. 2009). Because this sample is apparent magnitude limited ($m_r < 17.75$), in practice, by R–L relation we always mean $\log_{10}R$ fitted as a function of absolute magnitude (see Sheth & Bernardi 2012 for a simple description of the bias which would arise from fitting L as a function of R). And R denotes the radius which encloses half the total light L. (For exponential discs, this radius is 1.67 times the scalelength of the exponential. In the case of two components, R is a complicated function of the light in each component and the two scale radii.)

Our goal implies that we must fit the observed profiles and determine the associated R–L relation using a variety of different models. Section 2 summarizes the relevant properties of the SDSS DR7 sample we study. Section 3 provides an analysis of the light profiles of SDSS DR7 galaxies which we believe strongly suggests that fitting to a SerExp model returns the least biased answers. Section 4 compares the R–L relation based on single Sérsic, Sérsic + exponential, de Vaucouleurs + exponential, and single de Vaucouleurs fits, showing that the relations from single Sérsic fits (the standard to date) are offset to larger sizes and those from single de Vaucouleurs fits to smaller sizes, compared to those from the two-component fits.

There is no particular reason why systems supported by rotational motions should define the same R–L relation as those supported by random motions. Therefore, it makes little sense to speak of a single R–L relation for the entire galaxy population. Indeed, the R–L relation has long been known to depend on morphological type (e.g. Shen et al. 2003). Section 5 quantifies this morphological dependence, and then focuses on the differences between the relations defined by early-type bulge-dominated systems, and later type disc-dominated systems. Disc-dominated galaxies have small bulges, and bulge-dominated galaxies have extended second components. In Section 6 we use our Sérsic–exponential fits to study the $R_{\rm bulge}-L_{\rm bulge}$ relation of early types, $R_{\rm disc}-L_{\rm disc}$ of late types, and the ratio of the bulge size to that of the other component in both early and late types. Note that we do not distinguish between bars and bulges in late-type galaxies but none of our science goals depend on this distinction. A final section summarizes our findings.

2 THE SDSS DR7 SAMPLE

In this paper, we study the galaxies in the DR7 of the SDSS Main Galaxy sample (Abazajian et al. 2009). This sample contains $\sim 5 \times 10^5$ galaxies at $z \sim 0.1$, and is apparent magnitude limited to $m_r < 17.75$, where m_r is a Petrosian magnitude. This limit is sufficiently bright that surface brightness related selection effects are negligible.

The DR7 data base provides crude estimates of the (galactic extinction corrected) apparent brightness and angular size of each galaxy in the catalogue. We will use the SDSS-based `cmodel` magnitudes and sizes (a weighted combination of separate fits to exponential and de Vaucouleurs profiles) defined in Bernardi et al. (2010). When converting these to physical sizes and luminosities, we assume a flat Λ cold dark matter model with $\Omega_{\rm m} = 0.3$ and a Hubble constant whose present value is $H_0 = 70$ km s^{-1}Mpc^{-1}. The luminosities are k-corrected following Bernardi et al. (2003a). For colours we use SDSS DR7 `model` magnitudes (corrected for galactic extinction). The data base also provides estimates of the stellar velocity dispersion of each galaxy. We follow custom and correct these values for aperture effects following Bernardi et al. (2003a).

In the first half of this paper, we describe a number of other estimates of the total light associated with each r-band image (analysis of the images in other bands is ongoing). However, recent work has focused on stellar masses M_* rather than luminosity L. Our estimated stellar masses come from combining our estimates of L_r with (M_*/L_r) estimated following Bernardi et al. (2010) assuming a Chabrier initial mass function.

2.1 Estimates of photometric parameters

One of our primary goals is to quantify how the R–L relation depends on how R and L were estimated. To this end, we perform fits to the SDSS DR7 Main Galaxy Sample images using the PYMORPH

Downloaded from https://academic.oup.com/mnras/article/443/1/874/1471537 by guest on 08 December 2023

package, which can fit seeing convolved two-component models to observed surface brightness profiles (Vikram et al. 2010, see their figs 4–6 for a discussion of the steps involved, and choices made regarding e.g. the pixels to be masked, centring and alignment of the two components, etc.). The algorithm is described and tested in Meert, Vikram & Bernardi (2013) who show that when the fitted functional form is the same as the one used to generate the image, then PYMORPH returns accurate values of the free parameters (e.g. background sky level, total light, half-light radius, Sérsic index, axis ratio and bulge–total ratio).

We use PYMORPH to fit single component de Vaucouleurs and Sérsic profiles, and two component exponential + de Vaucouleurs (deVExp) and exponential + Sérsic (SerExp) profiles to each image. It is conventional to speak of the two components as being 'bulge' and 'disc' components; while this is accurate for disc-dominated systems (typically later type galaxies), it may be better to think of the 'disc' component in bulge-dominated systems (typically early-type galaxies) as simply being a second component that is not necessarily a (thin, inclined) disc (e.g. Oemler 1976; Schombert 1986; Gonzalez, Zabludoff & Zaritsky 2005).

Before moving on, we note that there is an analytic expression for the light enclosed within a given distance of the centre of a single circular Sérsic profile (e.g. Ciotti & Bertin 1999). From this, the half-light radius can be obtained easily. However, if the object has axis ratio $b/a \neq 1$, where b and a are the half-light radii along the principal axes of the image, then the corresponding expression must be integrated numerically. Since this can be time consuming, it is usual to approximate this case by using the expression for a circle, but with a suitably chosen effective circular radius. The most common choice is $\sqrt{ba} = a\sqrt{b/a}$, but Saglia et al. (2010) have recently shown that $(b + a)/2$ is more accurate: for bulge-dominated systems the difference matters little, but it does matter for discs. Therefore, we use $(b + a)/2$ except in Section 4.1 where, to fairly compare with previous work, we use $\sqrt{ba}$.

This raises the question of what we should do when we have two components? A natural choice would be to circularize each component using its own $(b + a)/2$, and to then determine the half-light radius of the sum of the circularized components, where each is weighted by the fraction of the total light that it contains (e.g. equation B3 in the appendix). We have found that this approximation is quite accurate, so we use it throughout.

2.2 Morphologies

A secondary goal of this paper is to quantify the role of galaxy type or morphology on the *R–L* relation. In practice this is difficult, because unambiguous determinations of the morphological type are not straightforward, although the task is slightly easier for bulge-dominated systems. Previous work has used crude proxies for morphological type: these include isophotal shape and central concentration (Strateva et al. 2001), the Sérsic index n (Shen et al. 2003), the colour, spectral features, and some combination of the above (Bernardi et al. 2003a; Baldry et al. 2004).

In what follows, we use the Bayesian Automated Classifications (hereafter BAC) of Huertas-Company et al. (2011) which are available for our full DR7 sample. The BAC are particularly interesting, because they are expressed as probabilistic weights (determined from an object's k-corrected $g - r$ and $r - i$ colours, and its isophotal shape and light concentration in the i band) – something we expect will become increasingly common in the next generation of large data sets. We explore the use of hard cuts based on these weights as indicators of morphology, as well as simply weighting each galaxy by the BAC probability that it is one type or another.

Table 1. Eyeball morphological classifications from F07. We set E ($T = 0$ and 0.5), S0 ($T = 1$), Sa ($T = 1.5$ and 2), Sb ($T = 2.5$ and 3) and Scd ($T = 3.5$, 4, 4.5, 5 and 5.5).

Selection	E	S0	Sa	Sb	Scd
EARLY TYPES					
Selected					
P(E+S0) > 0.85 AND $n > 3$	0.70	0.21	0.08	0.01	0
$n > 2.5$	0.44	0.18	0.20	0.13	0.05
Missed					
P(E+S0) < 0.85 OR $n < 3$	0.10	0.43			
$n < 2.5$	0.02	0.12			
LATE TYPES					
Selected					
P(E+S0) < 0.15 AND $n < 3$	0	0.01	0.08	0.36	0.51
$n < 2.5$	0.01	0.04	0.11	0.33	0.45
Missed					
P(E+S0) > 0.15 OR $n > 3$			0.86	0.47	0.21
$n > 2.5$			0.75	0.41	0.16

For instance, we will study an 'early-type' sample defined on the basis of hard conservative cuts on two parameters which are available for each galaxy: the value of n returned by PYMORPH when fitting a single Sérsic profile to the image, and the BAC probability p(E+S0) that the object is an early type. We require

$$n > 3 \qquad \text{and} \qquad p(\mathrm{E+S0}) > 0.85.$$

These cuts by no means select all early-type galaxies; they are simply designed to select a population which is very unlikely to be contaminated by later types. Since our goal is to select objects of a single type, we are willing to sacrifice completeness for purity.

To assess how these BAC-based hard cuts perform, we use the eyeball classifications of Fukugita et al. (2007, hereafter F07) and of Nair & Abraham (2010, hereafter N10). These are based on analysis of a much smaller patch of the SDSS sky, and a brighter magnitude limit (e.g. F07 has only ∼7000 objects restricted to $m_r < 16$; N10 has about twice as many), but for our purposes, the important point is that they are both magnitude limited.

Whereas BAC classifies galaxies into four (E, S0, Sab and Scd) morphological types, F07 use $0 < T < 7$ in steps of 0.5. To convert, we assign E ($T = 0$ and 0.5), S0 ($T = 1$), Sa ($T = 1.5$ and 2), Sb ($T = 2.5$ and 3) and Scd ($T = 3.5$, 4, 4.5, 5 and 5.5). Similarly, N10 use the T-type classification ($-5 < T < 7$) from the modified RC3 classifiers; we assign E ($T = -5$ and -4), S0 ($T = -3$, -2 and -1), Sa ($T = 0$, 1 and 2), Sb ($T = 3$ and 4) and Scd ($T = 5$, 6 and 7).

Table 1 shows the mix of F07 morphological types in samples which are defined by the hard cuts [on n and BAC p(type)] given above. Table 2 reports a similar analysis which is based on the eyeball classifications of N10 instead of F07. These tables show that 91 and 86 per cent of the resulting sample are indeed either E or S0. In contrast, requiring only $n > 2.5$ (as done in the past) yields a sample in which the E+S0 fraction is just 62 and 56 per cent, respectively. (A small fraction of the objects are irregulars, which is why the numbers do not always add up to 100 per cent.) Clearly our selection is much purer.

As a measure of its incompleteness, we also indicate the fraction of objects classified as Es and S0s which do not make the cut. These fractions are 10 and 43 per cent for the F07 classifications, and 14 and 43 per cent for N10. This 'missed' fraction is much smaller if

Downloaded from https://academic.oup.com/mnras/article/443/1/874/1471537 by guest on 08 December 2023

Table 2. Eyeball morphological classifications from Nair & Abraham (2010) who used T-type classification using the modified RC3 classifiers. We set E ($T = -5$ and -4), S0 ($T = -3$, -2 and -1), Sa ($T = 0$, 1 and 2), Sb ($T = 3$ and 4) and Scd ($T = 5$, 6 and 7).

Selection	E	S0	Sa	Sb	Scd
EARLY TYPES					
Selected					
P(E+S0) > 0.85 AND $n > 3$	0.57	0.29	0.14	0	0
$n > 2.5$	0.32	0.23	0.29	0.12	0.03
Missed					
P(E+S0) < 0.85 OR $n < 3$	0.14	0.43			
$n < 2.5$	0.02	0.07			
LATE TYPES					
Selected					
P(E+S0) < 0.15 AND $n < 3$	0	0	0.15	0.41	0.39
$n < 2.5$	0.01	0.03	0.17	0.35	0.36
Missed					
P(E+S0) > 0.15 OR $n > 3$			0.79	0.35	0.17
$n > 2.5$			0.71	0.33	0.10

we only require $n < 2.5$, but we believe the price to pay in purity is unacceptable.

The bottom halves of the two tables show a similar analysis of BAC and n cuts which are designed to produce a pure sample of later types. In this case requiring

$$n < 3 \qquad \text{and} \qquad p(\mathrm{E+S0}) < 0.15$$

yields a sample in which Sa + Sb + Scd account for 95 per cent of the objects. If we only require $n < 2.5$, and do not use the BAC probability at all, then Sa + Sb + Scd account for 89 per cent of the objects so, for later types, the use of the BAC analysis does not make such a dramatic difference.

Whereas the extremes of the morphological mix are relatively easy to define, Tables 1 and 2 indicate that the intermediate regime, the Sa/Sb class, will be difficult to define cleanly. Indeed, we have found that more than a third of the objects with BAC $p(\mathrm{S0}) > 0.6$ are Sas, and about a fifth of the objects with $p(\mathrm{Scd}) > 0.6$ are Sbs. Conversely, of the objects which have $p(\mathrm{Sab}) > 0.6$, about one third are Scds. For this reason, when we provide these BAC weight-derived relations in Tables 3 and 4, we refer to them as being for E, S0/Sa, Sa/Sb/Scd and Scd samples.

We will use these hard cuts, as well as the BAC weights themselves, in Section 4. Note that all the results which follow are based on the full SDSS DR7 sample: we use the smaller F07 and N10 samples again only to perform sanity checks (as we did here) in Section 5.

3 SERSIC INDEX AND B/T RATIO IN SDSS GALAXIES: EVIDENCE FOR TWO COMPONENTS IN THE SURFACE BRIGHTNESS PROFILE

In this section, we provide an analysis of the light profiles of SDSS DR7 galaxies which we believe strongly suggests that fitting to a SerExp model returns the least biased answers.

3.1 How many components?

As we noted in Section 1, it is not a priori obvious whether one or multiple components are physically reasonable or necessary. One way to address this question is to fit the image with the sum of two Sérsic profiles, each with its own value of n, and then see if allowing for the second component does indeed provide a statistically significant improvement in the accuracy of the fit (once one accounts for the increase in the number of fitted parameters). In what follows we will perform a slightly simpler version of this: we force one of the components to have $n = 1$, while leaving the other to be determined by the fitting procedure. We then provide a novel argument which

Table 3. Luminosity–size relation. Early types: $p(\mathrm{E+S0}) > 0.85$ and $n > 3$. Late types: $p(\mathrm{E+S0}) < 0.15$ and $n < 3$. Early-type bulges: the bulge half-light radius versus the bulge luminosity for galaxies with $p(\mathrm{E+S0}) > 0.85$ and $n > 3$. Late-type discs: the disc half-light radius versus the disc luminosity for galaxies with $p(\mathrm{E+S0}) < 0.15$ and $n < 3$.

Sample/fit	p_0	p_1	p_2
Sérsic (early types)	12.8145	1.3788	0.0377
Sérsic (late types)	8.4847	0.9092	0.0254
Sérsic ($n > 2.5$)	8.1624	0.9821	0.0292
Sérsic ($n < 2.5$)	4.7207	0.5601	0.0173
Sérsic (E)	7.0946	0.8650	0.0262
Sérsic (S0/Sa)	10.9232	1.2218	0.0344
Sérsic (Sa/Sb/Scd)	13.9656	1.4694	0.0395
Sérsic (Scd)	12.6494	1.3128	0.0352
SersExp (early types)	8.6032	0.9979	0.0290
SersExp (late types)	7.3204	0.7929	0.0226
SersExp ($n > 2.5$)	6.0716	0.7770	0.0242
SersExp ($n < 2.5$)	4.2848	0.5151	0.01615
SersExp (E)	7.4437	0.8922	0.0266
SersExp (S0/Sa)	9.6010	1.0903	0.0311
SersExp (Sa/Sb/Scd)	9.3135	1.0182	0.0286
SersExp (Scd)	7.8056	0.8396	0.0237
SersExp (early-type bulges)	−2.0733	0.0956	0.0098
SersExp (late-type disks)	6.4982	0.6934	0.0199

Table 4. Luminosity–size relation. Early types: $p(\mathrm{E+S0}) > 0.85$ and $n > 3$. Late types: $p(\mathrm{E+S0}) < 0.15$ and $n < 3$. Early-type bulges: the bulge half-light radius versus the bulge luminosity for galaxies with $p(\mathrm{E+S0}) > 0.85$ and $n > 3$. Late-type discs: the disc half-light radius versus the disc luminosity for galaxies with $p(\mathrm{E+S0}) < 0.15$ and $n < 3$.

Sample/fit	p_0	p_1	p_2
Sérsic (early types)	19.0933	−3.9536	0.2070
Sérsic (late types)	13.0054	−2.6438	0.1393
Sérsic ($n > 2.5$)	14.4995	−3.1767	0.1742
Sérsic ($n < 2.5$)	8.6098	−1.8301	0.1014
Sérsic (E)	13.6593	−2.9799	0.1635
Sérsic (S0/Sa)	20.1092	−4.1549	0.2166
Sérsic (Sa/Sb/Scd)	22.3082	−4.4655	0.2275
Sérsic (Scd)	17.9815	−3.6102	0.1862
SerExp (early types)	13.4131	−2.9324	0.1607
SerExp (late types)	11.2699	−2.3026	0.1227
SerExp ($n > 2.5$)	12.5026	−2.7875	0.1551
SerExp ($n < 2.5$)	9.5210	−1.9963	0.1090
SerExp (E)	12.8394	−2.8246	0.1557
SerExp (S0/Sa)	19.2830	−3.9866	0.2079
SerExp (Sa/Sb/Scd)	18.6150	−3.7425	0.1922
SerExp (Scd)	11.7537	−2.3957	0.1271
SerExp (early-type bulges)	4.0853	−1.4159	0.0992
SerExp (late-type discs)	17.9763	−3.5683	0.1831

Downloaded from https://academic.oup.com/mnras/article/443/1/874/1471537 by guest on 08 December 2023

indicates that this SerExp model is indeed a better approximation to the surface brightness profiles of real galaxies than is either a single Sérsic, or the deVExp model.

We are not the first to have come to this conclusion; e.g. Allen et al. (2006) argued that at least half of the $\sim 10^4$ galaxies at $z \sim 0.1$ in the Millennium Galaxy Catalog are two-component SerExp systems, and Simard et al. (2011) have recently performed a similar analysis of $\sim 10^6$ SDSS galaxies. But our argument for why we believe two components are needed is new.

To gain intuition, Section 3.2 shows the result of fitting a variety of synthetic images (generated using either a single- or two-component models) with single Sérsic, deVExp and SerExp profiles. Section 3.3 presents a similar analysis of SDSS DR7 galaxies. Section 3.4 discusses some biases which arise from fitting the image with a single Sérsic.

3.2 Fits to synthetic images

In this section, we show the result of using PYMORPH (Meert et al. 2013) to fit a variety of synthetic (mock) and real (SDSS) galaxies. We contrast what happens when PYMORPH is forced to fit an image using only a single Sérsic component, to when it is allowed to use two Sérsic components, one with $n = 1$ and the other free: the SerExp model. For the two-component fits, we first show results when n of the Sérsic component is set to 4, since this corresponds to the traditional 'de Vaucouleurs bulge + exponential disc' deVExp fits, and then when n is allowed to be a free parameter, determined by the fit.

In all the results which follow, the parent distribution is essentially a random subset of the SDSS DR7 main galaxy sample, which is magnitude limited to $m_r < 17.7$. We fit each object in this sample using three different models: a single Sérsic, a deVExp and a SerExp. We then use the best-fitting parameters from these different fits to generate three synthetic images for each object. In this way, we have, in effect, three different mock SDSS catalogues (see Meert et al. 2013 for detailed tests). If galaxies were, in reality, e.g. two-component deVExp models, then only our deVExp mock catalogue would be realistic – performing profile fits (e.g. using the other two models) to this catalogue should return results which are similar to those when fitting to the SDSS data. Moreover, although all three catalogues will contain correlations between n, total luminosity, half-light radius, etc. these correlations are only guaranteed to be like those in the SDSS data for this (in this case, deVExp) mock catalogue.

3.2.1 *Fitting to a profile which is truly a single Sérsic*

We begin with the case in which PYMORPH is asked to fit what is in reality a single Sérsic profile of index n (i.e. we use the mock galaxies generated using a single Sérsic profile) with a single component Sérsic, and with deVExp and SerExp profiles. The distribution of input n values used to simulate the mock galaxies is that which one obtains from fitting single Sérsics to the parent (magnitude limited) sample. Rather than showing the fits themselves, we present our results in the parameter space of the best-fitting n versus best-fitting B/T. In all cases, darker shading indicates regions in the parameter space that are more heavily populated.

The top row in Fig. 1 shows results for input single Sérsic mock galaxies. The two panels on the left show B/T values determined from the deVExp fits, and the two on the right are from SerExp fits. We describe the deVExp results first. The top-left panel in Fig. 1 shows the distribution of the sample in best-fitting $n - B/T$ space, and the next panel to the right shows the result of restricting the analysis to narrow ranges of input n. The different colours show the distribution in fitted n and B/T for input n in the range 0−2, 2−4, 4−6 and 6−8 (we show the regions which enclose 25, 50 and 75 per cent of the points). Comparison with the values along the y-axis shows that PYMORPH correctly returns the input n values.

The distribution in the $n - B/T$ plane is clearly non-trivial. For $n < 4$, there is a tight correlation between the value of n returned by the single component and B/T from the de Vaucouleurs-exponential fit: $B/T \to 1$ as $n \to 4$. But as n increases beyond 4, B/T begins to decrease again. That is, B/T is not a monotonic function of n. Since the deVExp profile only has $n = 1$ or 4 components, to fit $n > 4$ profiles PYMORPH requires more and more of an exponential-like component, i.e. B/T decreases. (The figure does not show this, but the fit returns bulge half-light radii which are ever smaller fractions of the half-light radius of that of the input Sérsic profile.) As a result, for $1/2 < B/T < 1$, the distribution of n at fixed B/T appears bimodal. This shows that, unless one is certain that large values of n do not occur in nature, then, especially around $B/T \sim 0.7$, B/T values may be misleading, if not meaningless.

The two panels on the right show the corresponding distribution for SerExp; they are clearly different from those for deVExp. This is primarily because PYMORPH correctly assigns the entire profile to the bulge (Sérsic) component, except when the input $n \sim 1$, since then which of the two $n = 1$ components should be called the bulge is ambiguous. (We have checked that, when $n \sim 1$ and $B/T < 1$, then the half-light radius of the 'bulge' component is indeed the same as that of the total, i.e. the two components differ only by the value of B/T.) The fact that B/T is not exactly equal to unity is a measure of the error in B/T which comes from the extra degree of freedom associated with having a second component with which to fit the profile.

3.2.2 *Fitting to a profile which is truly a deVExp*

The second row shows results when the input profile used to simulate the mock galaxies is a two-component deVExp model (the distribution of input B/T values is obtained from fitting deVExp models to the SDSS parent magnitude limited sample). This two-component profile is then fitted with a single Sérsic to get n; B/T comes from fitting a deVExp model (two panels on left) or a SerExp model (two panels on right). The overall (grey-scale) distributions are rather different than in the corresponding panels in the top row. This is the first hint that the distribution of fitted n–B/T can be used as a diagnostic of the true profile shape. Different colours show results for narrow bins in input B/T; these indicate that PYMORPH indeed returns the correct values when it fits the right-hand model. The additional freedom when fitting a SerExp profile to what is really a deVExp means that, in the panel on the far right, the distribution of fitted B/T at fixed input B/T is slightly broader than when fitting a deVExp.

3.2.3 *Fitting to a profile which is truly a SerExp*

Finally, the bottom row shows results when the input model used to simulate the mock galaxies was a SerExp (with n and B/T values chosen from fitting the SDSS parent sample to a SerExp model). The results here differ from those in the row above in subtle ways, perhaps most appreciably in the upper-right corner (large fitted n and B/T) of the bottom-right plots.

Downloaded from https://academic.oup.com/mnras/article/443/1/874/1471537 by guest on 08 December 2023

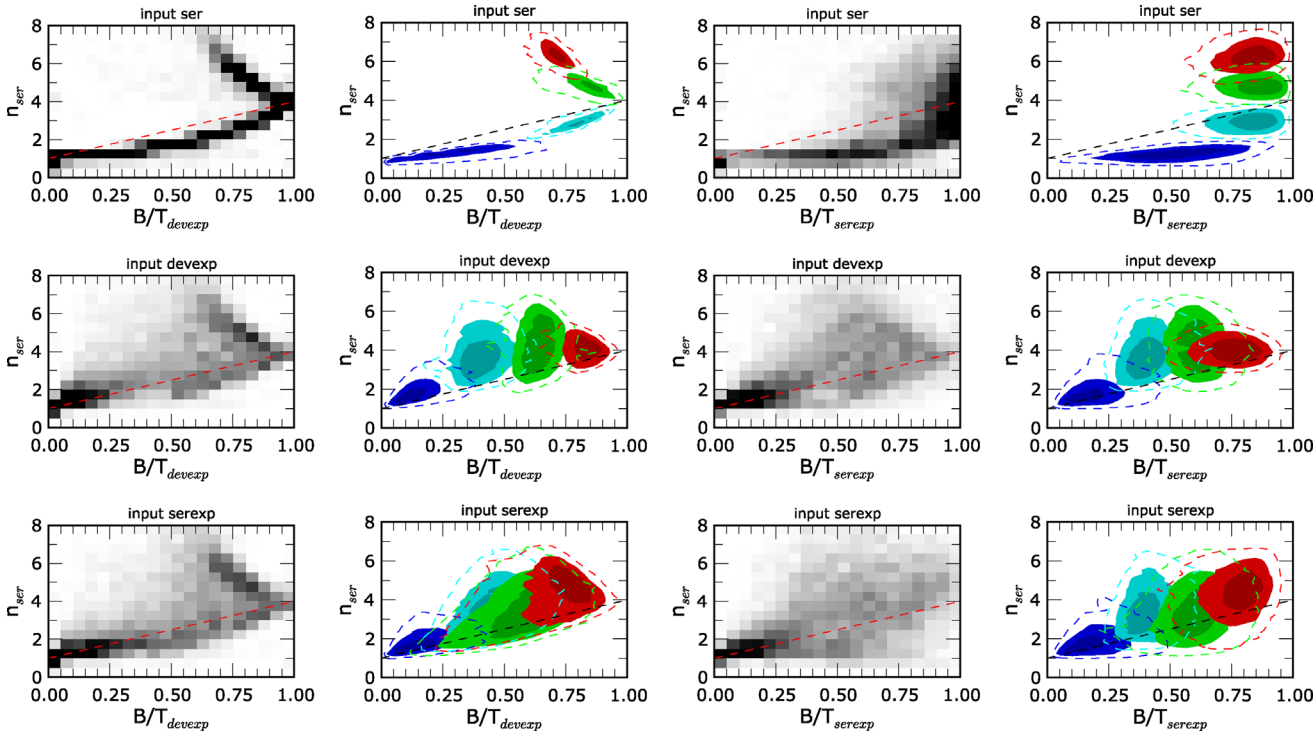

Figure 1. Fitted $n_{\rm ser}$ versus fitted B/T for simulated images which were generated using a single component Sérsic profile (top), or two-component deVExp (middle) or SerExp profiles (bottom). The two left-hand columns show $n_{\rm ser}$, returned by fitting a single Sérsic profile to the image, versus B/T, returned from fitting a deVExp profile; the two right-hand columns show the same $n_{\rm ser}$, but now B/T comes from a SerExp fit. For each pair of columns the left-hand column shows the density across the full sample, while the right-hand column shows the density for four bins, coloured by input $n_{\rm ser}$ (top; the bins have width $\Delta n_{\rm ser} = 2$ and run from 0to8, with red showing the largest $n_{\rm ser}$) and input B/T (middle and bottom; bins have width $\Delta B/T = 0.25$ and run from 0 to 1 with red showing the largest B/T). For each colour, the darkest region contains 25 per cent of the sample, the lighter region surrounding it contains 50 per cent, and the outermost dashed line contains 75 per cent of the sample. The straight dashed line, same in each panel, serves mainly to guide the eye, and to facilitate comparison between panels. Clearly, the distribution of $n_{\rm ser}$ versus B/T depends on the input model.

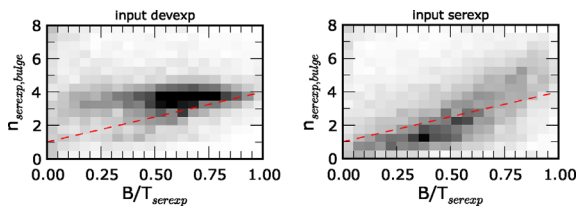

Figure 2. Parameters $n_{\rm ser}$ of the bulge and B/T obtained from fitting the two-component SerExp model to mock galaxies generated using input deVExp (left) and SerExp models (right). In the panel on the left, the fits correctly return values of $n_{\rm ser} \sim 4$; in the panel on the right, the distribution resembles the input one: notice that this one indicates that bulges do not necessarily have $n = 4$. The red dashed line, same in both panels, serves only to guide the eye.

In this case, we also show (Fig. 2) the $n_{\rm bulge}-B/T$ plane, where both $n_{\rm bulge}$ and B/T come from fitting a SerExp model to mock images generated using input deVExp (left) and SerExp (right) profiles. The panel on the left shows that PYMORPH correctly returns $n \sim 4$ when it should; we have checked that the distribution in the panel on the right is similar to the input one, again suggesting that PYMORPH is working well (Meert et al. 2013).

3.3 Fitting to SDSS images

Fig. 3 shows a similar analysis of SDSS images. In the two panels on the left, n comes from fitting a single component Sérsic, and B/T from fitting a two-component deVExp. In the panels on the right, B/T comes from fitting a two-component SerExp. Notice that the grey-scale plots are very unlike those in the top row in Fig. 1, and most like those in the bottom row. This suggests that SDSS galaxies are almost certainly not single component systems.

In addition, of the two-component models, the SerExp model appears to be more like the data than is the deVExp. This is because, when B/T comes from fitting a SerExp, then the SDSS data (third panel from left) populate the large $n - B/T$ corner which input SerExp models also fill, but input deVExp models do not (cf. Fig. 1). There is a more subtle difference when B/T comes from the deVExp fit (left most panels) in Figs 1 and 3: the SDSS shows a rather well-defined ridge at the boundary of the large $n-B/T$ corner, which appears to be more separated from the peak at small n. This separation is more apparent for the input SerExp models than for input deVExp.

Since we cannot classify the objects by the true value of n or B/T, the colours (contours in Fig. 3) show the result of restricting the analysis to objects which are most likely to be early types (red) to least likely (blue), as determined by Huertas-Company et al. (2011). This shows that the early types do indeed have large values of n, and spirals the lowest, as expected.

To provide a slightly more straightforward comparison between simulations and data, we have considered the $n-B/T$ distribution for objects in narrow bins in (output) luminosity. Figs 4 and 5 show results in simulations (the same fits used for Fig. 1) and in the SDSS (cf. Fig. 3), respectively. These too indicate that the two-component models are more like the data, with the SerExp marginally favoured

Downloaded from https://academic.oup.com/mnras/article/443/1/874/1471537 by guest on 08 December 2023

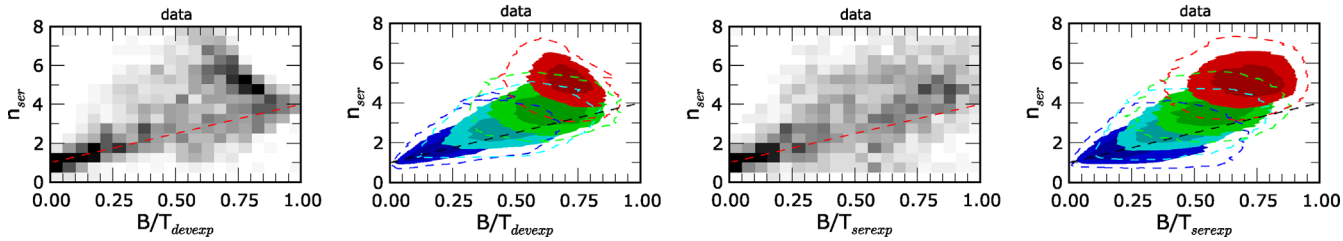

Figure 3. Similar to Fig. 1 but for real galaxies. Fitted (single component) $n_{\rm ser}$ versus fitted B/T using the two-component deVExp fit (two left-hand columns) and the two-component SerExp fit (two right-hand columns). Colours represent the probability that the galaxy is an early type (four adjacent bins in p(E+S0) bins, each of width 0.25, with red showing the highest probability bin). Comparison with the previous figure shows greatest agreement with the row of bottom panels in which the input model was a two-component SerExp.

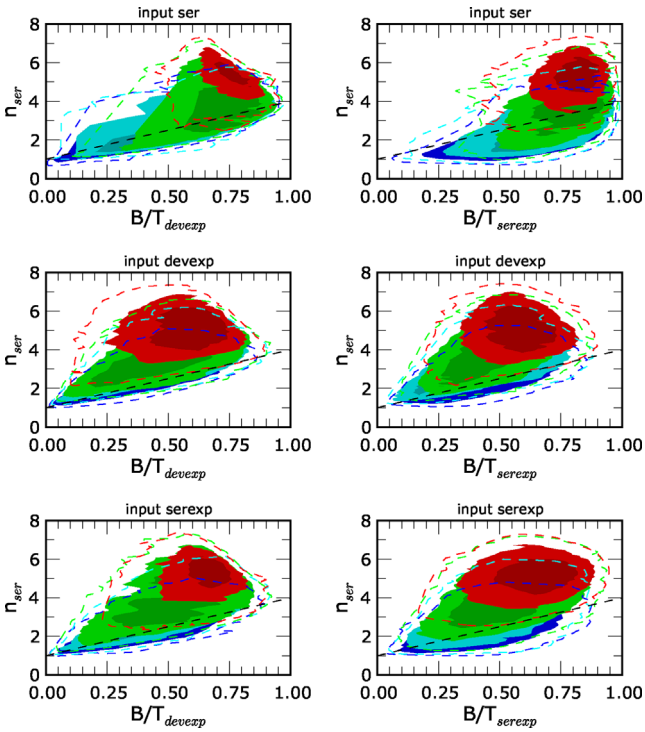

Figure 4. Fitted $n_{\rm ser}$ versus fitted B/T for simulated galaxies that are assumed to be single Sérsic profiles (top), two-component deVExp profiles (middle) and two-component SerExp profiles (bottom). In all cases, the y-axis shows $n_{\rm ser}$ returned by fitting a single Sérsic profile to the image. In the left-hand column, B/T is obtained from fitting a two-component deVExp model; in the right-hand column, B/T is determined from fitting a SerExp model. The density is shown in four bins coloured by output absolute magnitude: $-24 < M_r < -23$ (red), $-23 < M_r < -22$ (green), $-22 < M_r < -21$ (cyan) and $-21 < M_r < -20$ (blue). The top panel is clearly rather different from the other two.

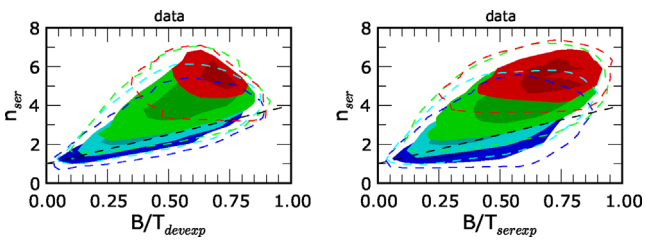

Figure 5. Similar to Fig. 4 but for real SDSS galaxies. These data are most similar to the bottom panel in Fig. 4, for which the input model was a two-component SerExp profile.

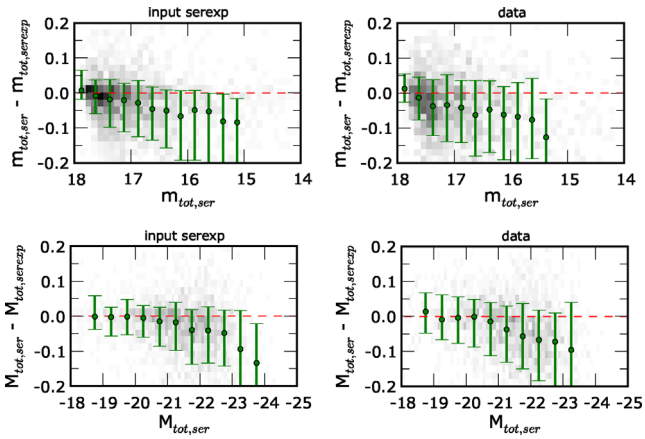

Figure 6. Comparison of total apparent magnitude (top) and luminosity (bottom) returned from single Sérsic and SerExp fits to simulated SerExp (left) and real SDSS (right) galaxies. The error bars show the 1σ rms scatter around the median. The similarity between the panels on the left with their counterparts on the right indicates that the input SerExp model is realistic.

(the two panels in Fig. 5 look more like the bottom than the middle panels in Fig. 4).

3.4 Biases from fitting single Sérsic profiles

The analysis above shows that a single component Sérsic profile is not as good a description of SDSS galaxies as one with two components. Since such single component fits are much simpler to perform, and are commonly used, it is interesting to ask if they lead to significant biases in commonly used parameters. For example, one might expect the total light to be a reasonably robust quantity, so different models for the shape of the profile may still return consistent values of $L_{\rm tot}$.

The top-left panel in Fig. 6 shows that the apparent magnitudes returned by single Sérsic fits to the objects in our SerExp mock catalogue are quite accurate, with a tendency for the Sérsic fits to return an overestimate by about 10 per cent at the bright end. The top-right panel shows that a similar comparison for the objects in the SDSS produces similar results. The bottom panels show the impact of these small biases on the inferred luminosities.

Fig. 7 shows a similar analysis of the half-light radii: the single Sérsic fit tends to overestimate the sizes by about 10/15 per cent, particularly for the largest objects. The largest and/or most luminous galaxies tend to have large n and/or intermediate to large B/T. Therefore, this bias is worst for objects that are likely to be ellipticals. We show this explicitly in Fig. 8.

Downloaded from https://academic.oup.com/mnras/article/443/1/874/1471537 by guest on 08 December 2023

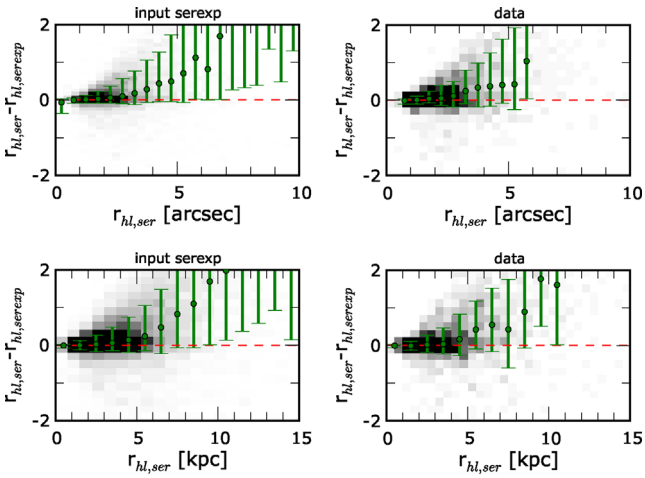

Figure 7. Comparison of angular (top) and physical (bottom) half-light radii returned from single Sérsic and SerExp fits to simulated SerExp (left) and real SDSS (right) galaxies. The error bars show the 1σ rms scatter around the median. As for the previous figure, the similarity between the panels on the left with their counterparts on the right indicates that the input SerExp model is realistic.

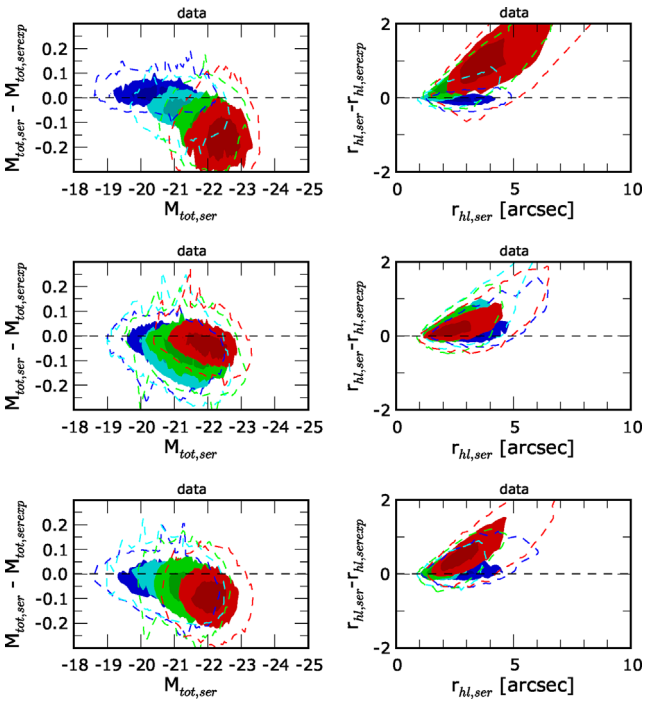

Figure 8. Comparison of luminosities (left) and angular half-light radii (right) returned from single Sérsic and SerExp fits to real SDSS galaxies, colour coded by best-fitting n (top), best-fitting B/T (middle) and $p(\mathrm{E+S0})$ (bottom). The single Sérsic-based luminosities are systematically brighter at the bright end; this bias is most pronounced when the best-fitting n is large. The single Sérsic sizes are larger if $n > 4$, $B/T > 0.5$ or $p(\mathrm{E+S0}) > 0.75$.

Fig. 9 illustrates the magnitude of such biases which come from forcing PYMORPH to fit single Sérsic and two-component SerExp models to what is truly a single Sérsic (left) or SerExp (right) profile. These show that when PYMORPH fits the right-hand model, it tends to return unbiased estimates. However, biases do arise when fitting an incorrect model, especially at high luminosities.

This raises the question of whether we should pay more attention to the panels on the left or the right? Since the SerExp model is a better description of the population as a whole than is a single Sérsic (Section 3.3), we are most interested in the panels on the right in Fig. 9. These show that fitting a single Sérsic to what is really a SerExp results in overestimates of the total luminosity and size, especially at the bright end. These biases have small systematic effects on the size–luminosity correlation of objects that are likely to be early types, and are presented in the next section. In contrast, late-type objects are less likely to be biased.

4 THE *R–L* RELATION AT $Z \sim 0.1$

We now study how the *R–L* relation depends on the functional form for the surface brightness profile that was assumed when estimating *R* and *L*. We would especially like to compare the effects of fitting one versus two-component models to the images, and we do this separately for the early- and late-type samples defined by the hard cuts on n and BAC p(type) described in Section 2.2.

4.1 Single Sérsic fits and comparison with previous work

To connect with previous work, we begin with a comparison of the PYMORPH derived *R–L* relation based on single Sérsic-derived parameters, with analogous fits from the literature. Using the objects in an earlier SDSS data release, Shen et al. (2003) reported fits to the *R–L* relation for objects which had $n > 2.5$ and $n < 2.5$, where *R*, *L* and n were determined from a single Sérsic fit to the light profile. Note that the Sérsic parameters used by Shen et al. were estimated from a one-dimensional radial surface brightness profile (`profMean`), measured in $\sim 5-10$ azimuthally averaged annuli (Blanton et al. 2003). Thus, it is expected to be significantly less accurate than a two-dimensional fit to the whole galaxy image.

The Shen et al. relations for $n > 2.5$ and $n < 2.5$ are shown as the dashed and dotted lines in the left- and right-hand panels in Fig. 10, respectively. The red and blue symbols with error bars show our determination of the single Sérsic based relation, where now *R*, *L* and n are from our PYMORPH reductions, and the grey symbols and error bars show the *R–L* relation which follows from single Sérsic fits performed by Simard et al. (2011, hereafter S11).

For objects with $n < 2.5$, the S11-derived relation runs parallel to that from Shen et al., but is offset to larger sizes by 0.05 dex, whereas the PYMORPH-derived relation transitions from Shen et al. at low luminosities to S11 at high luminosities. For objects with $n > 2.5$ the PYMORPH-derived relation lies about 0.1 dex above, and is more curved than the fit reported by Shen et al. The PYMORPH and S11 based relations depart significantly from Shen et al. at the low and high luminosity ends, where they curve upwards to larger sizes. For this reason, we are inclined to conclude that, at least at the bright end, Shen et al. are slightly biased. At the low end the curvature could be due to contamination by later type galaxies.

However, at the highest luminosities, and for objects with $n > 2.5$, the PYMORPH and S11 relations are also slightly but significantly different from one another. Appendix A shows that, in fact, at high luminosities, the derived magnitudes and sizes can be quite different: the correlated nature of these differences means that the *R–L* relation is only moderately affected. Appendix A goes on to show that the S11 reductions appear to require rather dramatic evolution in n and *R*: both are larger at $z = 0.2$ than at $z = 0.05$. Since we believe this is unphysical, we conclude that the PYMORPH reductions, which show no such systematic trend with z, are less biased, so we will use them in the remainder of this paper.

Downloaded from https://academic.oup.com/mnras/article/443/1/874/1471537 by guest on 08 December 2023

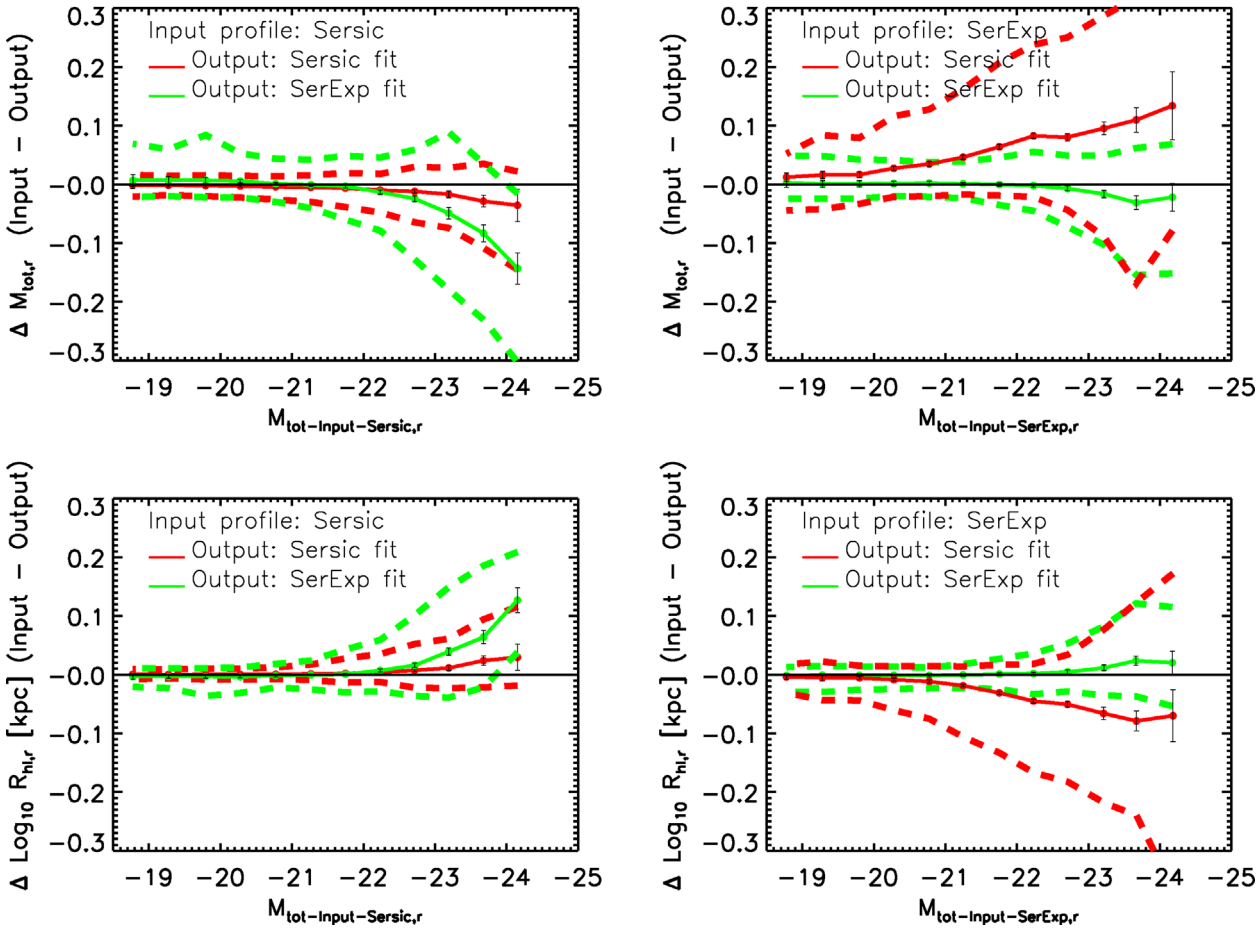

Figure 9. Biases in the estimated luminosities and sizes which come from fitting single Sérsic and two-component SerExp profiles to images which are really pure Sérsics (left) and two-component SerExps (right). The latter shows that fitting a single Sérsic to what is really a SerExp results in an overestimate of the total luminosity and size.

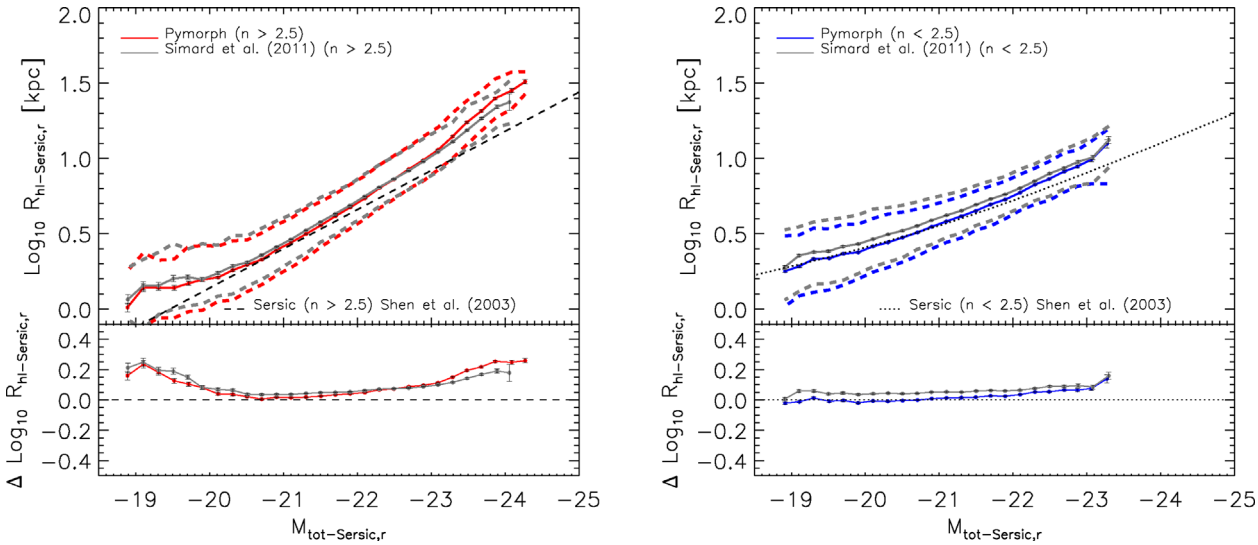

Figure 10. The r-band single Sérsic based half-light radius ($R_{\rm hl}$) versus total absolute magnitude ($M_{\rm tot}$) relation for objects with $n > 2.5$ (left) and $n < 2.5$ (right). In the panel on the left, our PYMORPH determination is in good agreement with that based on single Sérsic parameters from S11, but lies about 0.1 dex above, and is more curved than the fit reported by Shen et al. (2003). Symbols with error bars (joined by a solid curve for clarity) show the median half-light radius in bins of absolute magnitude. The dashed lines show the 16th and 84th percentile. In the panel on the right (objects with $n < 2.5$), except for the brightest objects, the PYMORPH relation lies systematically 0.05 dex below that of S11.

Downloaded from https://academic.oup.com/mnras/article/443/1/874/1471537 by guest on 08 December 2023

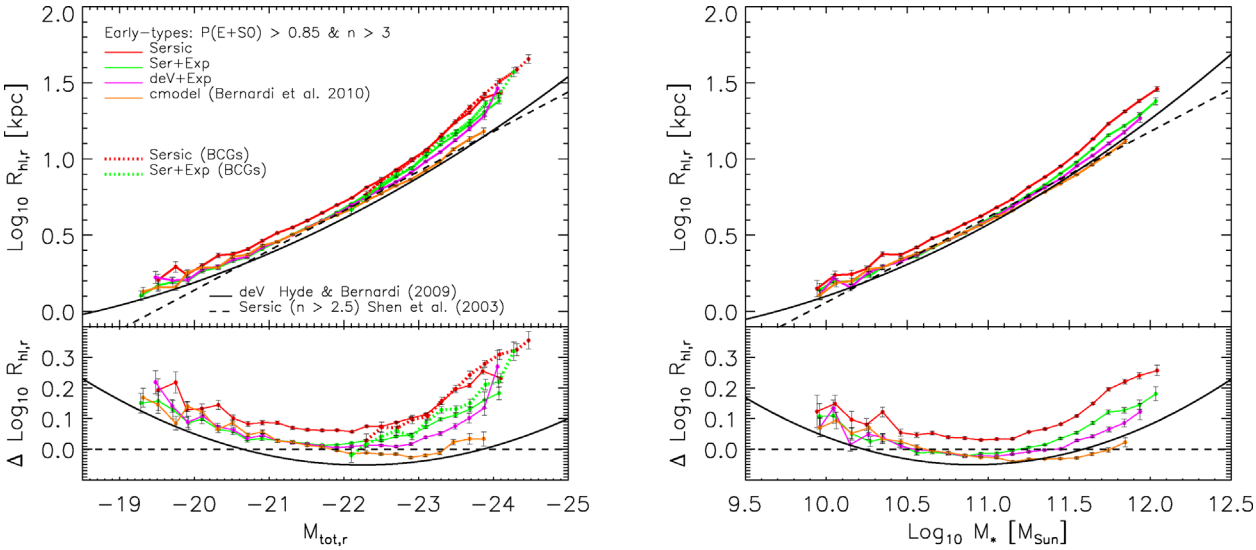

Figure 11. Dependence of derived size–luminosity (left-hand panels) and size–stellar mass (right-hand panels) correlations for early-type galaxies on the assumed surface brightness profile. Symbols with error bars (joined by a solid curve for clarity) show the median half-light radius in bins of absolute magnitude (left) and stellar mass (right). The SDSS fits to a single de Vaucouleurs profile return a relation with the smallest sizes; our PYMORPH fits to a single Sérsic profile return the largest sizes. Of the relations which lie in between these two extremes, and which are almost indistinguishable at $M < -21.5$, the SDSS based `cmodel` sizes (defined by Bernardi et al. 2010) are the smallest; those based on our PYMORPH fits to a two-component deVExp model are slightly larger; and those based on PYMORPH fits to a SerExp model are largest. The curvature at the bright end appears to be due to an increasing incidence of brightest cluster galaxies (BCGs), which define steeper relations (dotted lines) than the bulk of the early-type population. To highlight this curvature, bottom panel shows the ratio of all quantities in the top panel to the dashed line (Shen et al. 2003). The solid black line shows the fit reported by Hyde & Bernardi (2009).

4.2 Dependence on model fitting

Fig. 10 showed the *R–L* relation derived from single Sérsic fits to the two-dimensional surface brightness profile. We now compare these to relations based on SDSS fits to a single de Vaucouleurs profile; SDSS-based `cmodel` sizes defined by Bernardi et al. (2010):

PYMORPH fits to a two-component deVExp model; PYMORPH fits to a two-component SerExp model; and PYMORPH fits to a single Sérsic profile. As a result of the analysis in Section 3, we expect the SerExp reductions to return the least biased estimates of R and L, and hence of the *R–L* relation. We also show the corresponding R–M_* relations (with M_* estimated as described in Section 2).

All of these relations show curvature which we quantify by fitting to

$$\left\langle \log_{10} \frac{R}{\mathrm{kpc}} \middle| O \right\rangle = p_0 + p_1 O + p_2 O^2; \qquad (2)$$

the coefficients of these fits for $O = M_r$ and $O = \log_{10}(M_*/\mathrm{M}_\odot)$ are reported in Tables 3 and 4. Although p_1 is the coefficient of the linear part of the relation, the slope on scale O is $p_1 + 2p_2 O$; this is the value (at some characteristic O) which should be compared with the slope of a linear fit to the relation.

4.2.1 *Early types*

The panel on the left in Fig. 11 shows the *R–L* relation obtained for the early-type sample [i.e. $n > 3$ and $p(\mathrm{E+S0}) > 0.85$] based on a number of single and two-component fits to the images. There are clear systematic differences between these relations, with the single Sérsic and de Vaucouleurs models returning the relations with the largest and smallest sizes, respectively. The various two-component based relations are in good agreement except at the highest luminosities ($M_r < -22$), where the sample becomes increasingly contaminated by brightest cluster galaxies (BCGs) which are known to define steeper relations than the bulk of the population (e.g. Bernardi et al. 2007; Bernardi 2009).

The panel on the right shows a similar analysis of the R–M_* relation. Note that both *R–L* and R–M_* are significantly curved, consistent with previous work (e.g. Binggeli, Sandage & Tarenghi 1984, and the recent review by Graham 2013). Of course, if the stellar population models used to estimate M_*/L are incorrect, or if the IMF is mass dependent, then this will modify the curvature in R–M_*.

While not the main focus of this work, we note that Fig. 11 is consistent with recent work showing that a variety of other early-type galaxy scaling relations change slope at $\sim 3 \times 10^{10}\,\mathrm{M}_\odot$ and again at $\sim 2 \times 10^{11}\,\mathrm{M}_\odot$ (Bernardi et al. 2011a,b). Crude estimates of these two mass scales are given by the values of M_* at which a linear fit intersects the parabola given by the quadratic fit. For the SerExp fits to the early types shown above the best linear fit has $\langle R|M\rangle = -5.9155 + 0.598\log_{10}(M_*/\mathrm{M}_\odot)$, so it crosses the associated parabola (parameters from Table 4) at $\log_{10}(M_*/\mathrm{M}_\odot) = 10.4$ and 11.6. We could assign uncertainties to these scales by propagating the uncertainties on the fitted coefficients p_i, but these are smaller than the systematics associated with this particular choice of defining the mass scales. For example, another estimate comes from adjusting the amplitude of the straight line fit so that it is tangent to the parabola, and then identifying the scales on which the parabola lies sufficiently far from it. Fig. 12 shows such an analysis for the SerExp R–M_* relation; the vertical lines show 3×10^{10} and $2 \times 10^{11}\,\mathrm{M}_\odot$. This demonstrates our main point – that the existence of these two scales is not an artefact of the model used to estimate R and L.

4.2.2 *Comparison of early and late types*

We have repeated this analysis for the late-type sample [defined by requiring $n < 3$ and $p(\mathrm{E+S0}) < 0.15$]. Although we do not show

Downloaded from https://academic.oup.com/mnras/article/443/1/874/1471537 by guest on 08 December 2023

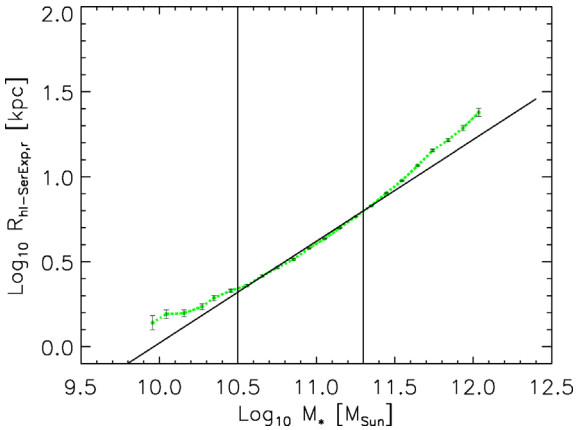

Figure 12. The R–M_* relation for SerExp fits, compared to a power law showing $R \propto M_*^{0.6}$. The vertical lines show the two mass scales identified by Bernardi et al. (2011a,b) on the basis of a variety of other early-type galaxy scaling relations; the R–M_* relation clearly curves away from the power law at these scales.

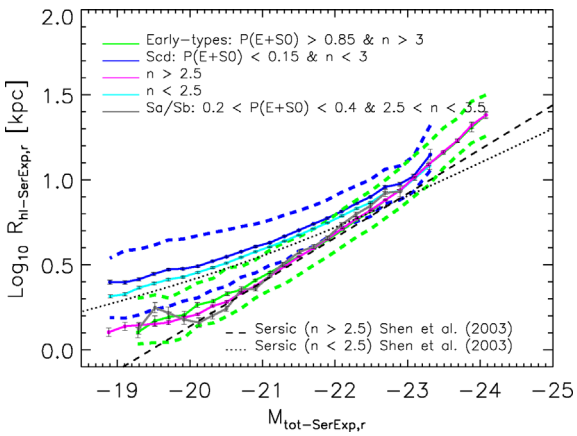

Figure 13. Similar to previous figure, but now objects are selected using different hard cuts which define early-, late- or intermediate-type (i.e. Sa/Sb) samples. Symbols with error bars (joined by a solid curve for clarity) show the median half-light radius in bins of absolute magnitude. The dashed lines show the 16th and 84th percentile. Note that this definition of intermediates (i.e. Sa/Sb) yields an R–L relation which is essentially the same as for the population with $n > 2.5$.

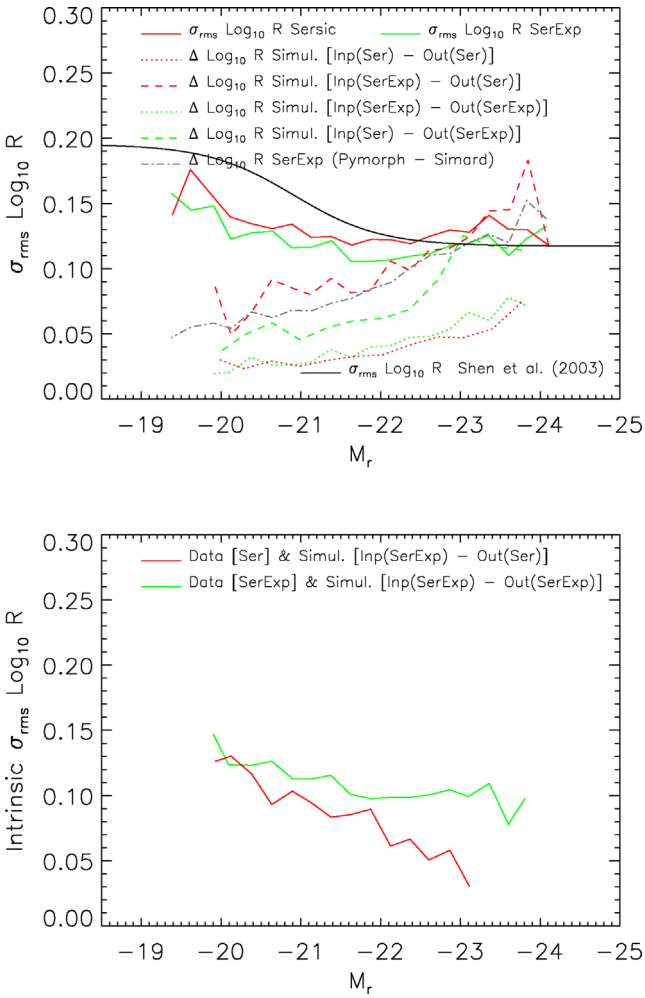

Figure 14. Top: observed scatter around the mean $\langle R|L\rangle$ relations for early types based on fitting Sérsic (solid red) and SerExp models (solid green) to the images. The black solid curve shows the corresponding (error-broadened) measurement from Shen et al. (2003). The dashed and dotted curves show a number of estimates from simulations of the measurement errors (see text for details). The grey dot–dashed line in top panel shows the rms difference between PYMORPH and S11 sizes (both based on fitting a two-component SerExp). Bottom: estimate of the intrinsic scatter around the Sérsic (lower, red curve) and SerExp (upper, green) derived relations for early types, obtained by subtracting in quadrature the red-dashed and green dotted curves from the corresponding red and green solid curves shown in the top panel.

the corresponding plots here, we again see curvature (coefficients of fits to equation 2 are given in Tables 3 and 4). Rather, we illustrate this in Fig. 13, which compares the SerExp-based R–L relation for our way of selecting early- and late-type samples, with the more traditional cuts on n (larger or smaller than 2.5). The two ways of selecting the samples lead to very similar results, with the low luminosity early types having smaller sizes, but defining a steeper relation, so they would cross the R–L relation of late types at about $M_r < -23$ (beyond which there are few late types anyway).

We have also selected an intermediate-type population (i.e. Sa/Sb) by requiring $2.5 < n < 3.5$ and $0.2 < p(\mathrm{E+S0}) < 0.4$. Notice that this sample defines the same R–L relation as when we require our early-type selection [i.e. $n > 3$ and $p(\mathrm{E+S0}) > 0.85$], as well as that when we only require $n > 2.5$; we return to this in Section 5.

4.3 Scatter in log(size) around the mean relation for early types

In addition to the mean R–L relation, the scatter around the mean relation is expected to constrain galaxy formation models (Shen et al. 2003; Shankar & Bernardi 2009; Shankar et al. 2012). As we show below, our analysis of the mean R–L relation allows us to make two interesting statements about the scatter around it for early-type galaxies: (i) there is intrinsic scatter and (ii) it is smaller at the high mass end.

The top two jagged solid curves in the top panel in Fig. 14 show the measured scatter around the mean R–L relation for SDSS early types, when R and L are determined by fits to a single Sérsic (larger scatter) and to a SerExp model (lower scatter). This scatter is broader than the intrinsic one, because it includes a contribution from the

Downloaded from https://academic.oup.com/mnras/article/443/1/874/1471537 by guest on 08 December 2023

measurement errors. For comparison, the smooth black curve shows the corresponding (error broadened) scatter reported by Shen et al. (2003). It is in reasonably good agreement with ours, except at the faint end, where we believe the enhanced scatter is due to increased contamination by spirals, for which the scatter is larger (as we show later).

To estimate the intrinsic scatter, we must account for the broadening due to measurement errors. We estimate the errors on the sizes from fitting to the objects in the mock catalogues used in Section 3, where we know the input values. (See Meert et al. 2013 for details of how the mocks were generated.) The dotted and dashed lines show these simulation-based estimates of the measurement error on the sizes for an early-type sample. The lowest dotted line shows the rms scatter in $\log_{10}R$ around the input value if the input profile is a single Sérsic, and we fit it with a Sérsic. In this, and all the cases which follow, we show this scatter as a function of the fitted (as opposed to the input) absolute magnitude. The other dotted line, which lies only slightly above the previous one, shows what happens if we fit a SerExp with a SerExp. These curves certainly underestimate the full measurement error, since they are based on fits to smooth images, whereas real images may be lumpy, have spiral arms, etc.

To get an idea of the magnitude of such effects, the dot–dashed curve in the top panel in Fig. 14 shows the rms difference between PYMORPH and S11 sizes returned by two-component SerExp fits to SDSS images, plotted as a function of the PYMORPH SerExp absolute magnitude for the early-type sample. This is almost certainly an overestimate of the measurement error on the sizes, since it includes systematic effects which arise from the differences between PYMORPH and S11; we have included it just to get a sense of the overall magnitude with which systematic rather than random errors might affect the scatter in the *R–L* relation.

The two dashed curves show results from using PYMORPH to fit a Sérsic with a SerExp (lower) and a SerExp with a Sérsic (upper). The differences between these and the dotted curves give an idea of the effect on the scatter of fitting an incorrect model to the data. The upper dashed curve is particularly interesting, in view of the fact that the SerExp model is more realistic (see Section 3), whereas the single Sérsic model is most often fit. Clearly, subtracting it in quadrature from the upper solid curve will lead to negative values at large luminosities. This is shown by the lower of the two curves in the bottom panel: at $M_r < -23$ or so, the intrinsic scatter is consistent with zero. This, of course, does *not* mean that the *R–L* relation is intrinsically a line with negligible scatter. Rather, it is entirely a consequence of fitting an incorrect model.

Recently, Nair, van den Bergh & Abraham (2011) have used just such an argument to claim that the *R–L* relation has no scatter. However, their argument is based on Petrosian sizes and luminosities; these are known to be inaccurate at large *L*, so the analysis above illustrates why their claim should be treated with skepticism. Indeed, the upper curve shows the result of subtracting (in quadrature) the upper dotted curve from the lower solid one, since both these are based on fitting to what we argued were more realistic models of the light profile (i.e. SerExp). In this case, the intrinsic scatter is well behaved: although it decreases steadily with M_r, it does not go negative.

Of course, since our estimate of the measurement error is really an underestimate, it is still possible that the intrinsic scatter is smaller than we show. Therefore, we turn to what we believe is a much more effective way of showing that there is some intrinsic scatter. This method studies if the residuals from the relation correlate with other parameters, once correlations between the measurement errors have

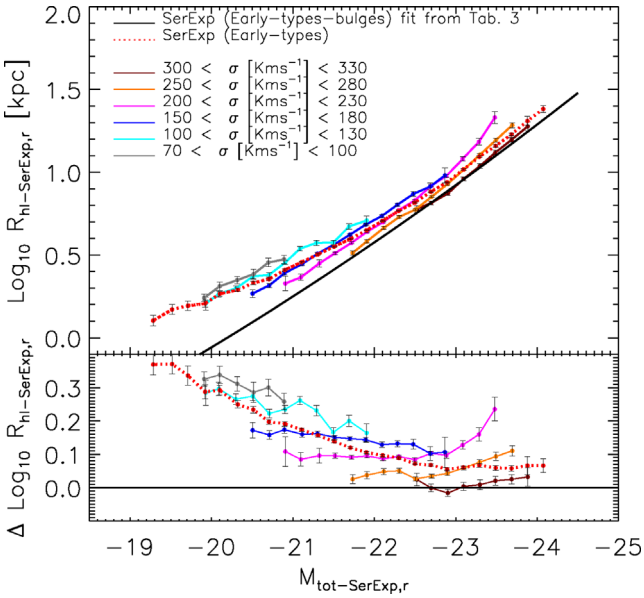

Figure 15. At fixed velocity dispersion σ, the *R–L* relation is almost a pure power law whose slope is almost the same for all σ (the black solid line shown is very close to $R \propto L^{0.83}$), but whose zero-point increases as σ decreases. In contrast, the relation upon averaging over all σ (red dotted curve) is much more curved. Bottom panel shows the result of dividing the measurements in the top panel by the black solid line.

been accounted for. If they do, then there must be some intrinsic scatter.

Fig. 15 shows the *R–L* relation for a number of narrow bins in velocity dispersion σ. At fixed σ, the *R–L* relation is a power law whose slope is 0.85 for all σ but whose zero-point increases as σ decreases. The scaling is quite well described by

$$\langle R|L,\sigma\rangle \propto L^{0.85}\sigma^{-0.73}. \quad (3)$$

The dependence on σ shows clearly that the scatter around the mean *R–L* relation correlates with σ; it is not all due to measurement errors. We are not the first to have made this point (see Bernardi et al. 2003b for an explicit discussion of this, although the long-studied Fundamental Plane is the result of this correlation), so it is surprising that Nair et al. ignored it. The slope of 0.85 (at fixed σ) is consistent with previous work (Bernardi et al. 2003a; Bernardi 2009). While steeper than the slope of 0.64 associated with averaging over all σ, it is less than unity – a fact we return to later, when we discuss the bulges of early types (see Fig. 22).

We end this subsection with the observation that the intrinsic scatter appears to be smallest for the most luminous objects. Since it is commonly believed that mergers will affect the scatter of scaling relations such as this one, our overestimate of the intrinsic scatter in the *R–L* relation provides a new constraint on models of how the most massive galaxies must have formed. For example, Shen et al. (2003) argue that many minor mergers may be more consistent with the shape and scatter of the *R–L* relation than are few major mergers. Other work has also explored constraints which come from the scatter (Shankar et al. 2012); it will be interesting to revisit this question in light of the mass dependence we believe we see.

Downloaded from https://academic.oup.com/mnras/article/443/1/874/1471537 by guest on 08 December 2023

5 DEPENDENCE ON BAYESIAN AUTOMATED CLASSIFIER MORPHOLOGIES

In the previous section, we used a hard cut on the BAC probability to determine morphology. Since this is not quite in the spirit of why such probabilities were generated in the first place, this section shows the result of using the BAC probabilities as weights when determining the *R*–*L* scaling relation. As this is one of the first such studies of weight-based scaling relations, and Tables 1 and 2 indicate that the relation between these weights and eyeball classifications can be complex in detail, we include an explicit comparison of these BAC-based scaling relations with those based on eyeball classifications.

Fig. 16 shows the size–luminosity (left) and size–M_* (right) relations obtained by weighting objects by p(type) as determined by BAC. The results of fitting equation (2) to these curved relations are reported in Tables 3 and 4.

Notice that galaxies weighted by p(Sab) define a relation which lies between that defined by p(Scd) on the one hand and p(E) and p(S0) on the other. However, the Sa/Sb class is difficult to define (cf. discussion of Tables 1 and 2). Fig. 16 reports the fraction of E, S0, Sa, Sb, Sbc and Irr galaxies classified by F07 with the corresponding BAC $p > 0.6$.

5.1 Comparison with eyeball classifications

To address this more closely, Fig. 17 shows the *R*–*L* relations in the F07 eyeball classified subsamples. The cyan curves show fits to these subsamples, and the magenta curves show fits based on the N10 (eyeball) classifications. The two are in quite good agreement. To emphasize the fact that the relation is different for the different subsamples, the red solid curve, which is the same in each panel, shows the BAC-based relation for p(E). The orange, green and blue curves (in the relevant panels) show the BAC-based relations for p(S0), p(Sab) and p(Scd). These are in good agreement with the F07 and N10 based relations for E and S0 galaxies.

Note that F07 and N10 agree that Sas define the same relation as Es and S0s, whereas Sbs are offset to larger sizes at smaller *L*. This suggests that combining Sas and Sbs into a single type may be problematic. Indeed, the BAC-based results for Sab lie further from that for Es compared to those based on F07 and N10 for Sas, but are in good agreement for Sbs; however, for Scds they lie closer to the E relation than do F07 or N10. These small but systematic differences between the BAC and eyeball based results suggest that combining Sabs into a single class as is done by BAC has resulted in a weighted sum of the relations defined by Es and Scds.

Fig. 17 shows that the curvature in the *R*–*L* relation is such that, for Scds, there is almost no correlation at $M_R > -20.5$. This flattening at low luminosities is also evident for the other morphological types, and is more pronounced in the *R*–M_* relation shown in the right-hand panel in Fig. 16 (see also Fig. 21 below). Indeed, Fig. 16 shows that at $\log_{10} M_*/\mathrm{M}_\odot < 10.5$, even the samples weighted by p(E) and p(S0) tend to have essentially no correlation between *R* and M_*. This is the same mass scale at which a number of other early-type galaxy scaling relations change qualitatively (Bernardi et al. 2011a,b and our Fig. 12). Since Figs 16 and 17 indicate that it also appears to be significant for late-type galaxies, it is interesting to ask if the other, higher mass scale identified by Bernardi et al., $M_* = 2 \times 10^{11}\,\mathrm{M}_\odot$, is also significant for late types.

Fig. 16 shows that, in fact, this higher mass scale seems to set the limit above which there are essentially no late-type galaxies. Fig. 17 tells a consistent story: although there are many Es and S0s brighter than $M_r = -23$, there are no Sa, Sb or Scds with luminosities this large. Bernardi et al. suggested that this mass scale was associated with merger histories that were dominated by major dry mergers; since such mergers would destroy discs, the fact that we see no late types above this mass scale is, perhaps, not surprising.

5.2 Small but statistically significant difference between ellipticals and S0s

Above, we noted that there is essentially one *R*–*L* relation for E, S0 and Sa galaxies. However, our sample is large enough to detect small but significant differences within the early-type (E and S0) sample. A closer look at Figs 16 and 17 indicates that S0s are slightly smaller than Es of the same luminosity. Fig. 18 shows that this offset is about 0.06 dex, although it depends slightly on how *R* and *L* were determined. This is particularly interesting in view of recent work at $z \sim 1$, based on the S11 reductions, which shows a

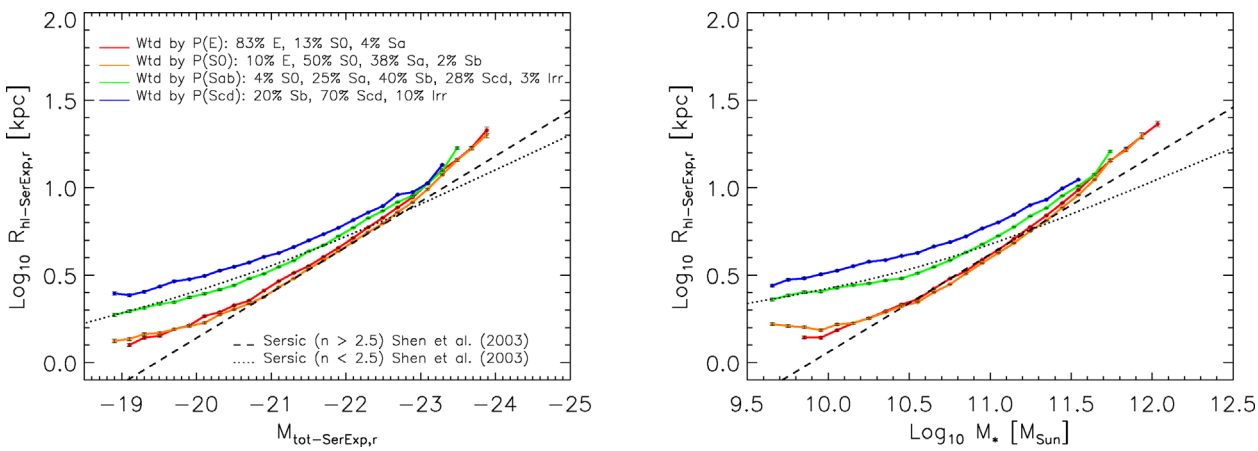

Figure 16. SerExp based size–luminosity (left) and size–M_* (right) relations, obtained by weighting objects by the BAC p(type). The low *L* or M_* part of the relation for Scds has the same slope as that reported by Shen et al. (2003) for their $n < 2.5$; and the intermediate *L* or M_* part has the same slope they report for $n > 2.5$. The relations for S0s are very similar to those for Es, and the Sab relations always lie between the E and Scd relations. Numbers in legend show the percentage of E, S0, Sa, Sb, Sbc and Irr galaxies classified by F07 with BAC $p > 0.6$. Using this selection we miss about 18 per cent of Es, 60 per cent of S0s, 64 per cent of Sab (37 per cent Sa and 27 per cent Sb) and 56 per cent of Scd, respectively.

Downloaded from https://academic.oup.com/mnras/article/443/1/874/1471537 by guest on 08 December 2023

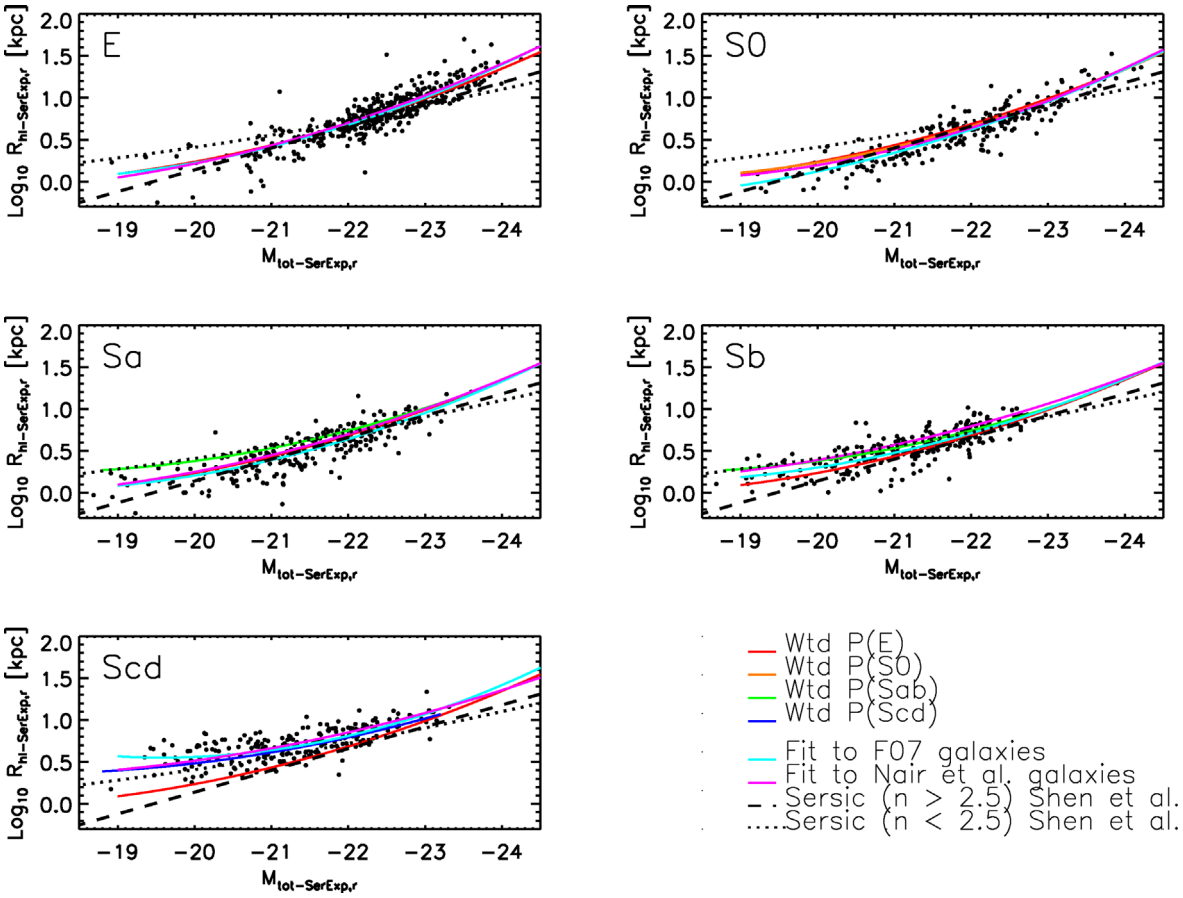

Figure 17. Comparison of the *R–L* relation in the morphologically defined samples of F07 (symbols and cyan curve) and N10 (magenta), with the fits defined by the BAC of Huertas-Company et al. (2011). All relations are in good agreement for E and S0 galaxies; for comparison, the E relation is also shown in the other panels. F07 and N10 agree that Sas define the same relation as Es and S0s, whereas Sbs are offset to larger sizes at smaller *L*. The BAC-based results for Sab lie further from that for Es compared to those based on F07 and N10 for Sas, but are in good agreement for Sbs; however, for Scds they lie closer to the E relation than do F07 or N10.

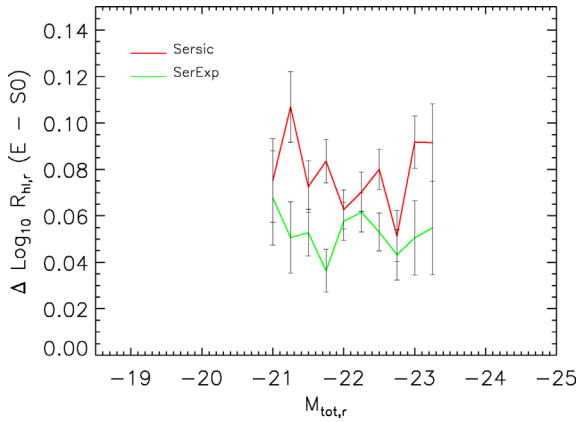

Figure 18. At fixed luminosity, Es tend to be about 0.06 dex larger than S0s, although this offset depends slightly on how *R* and *L* were determined.

similar offset of about 15 per cent for the SDSS sample growing to ∼40 per cent at $z \sim 1$ (Huertas-Company et al. 2012). Both the sign of the trend and its evolution deserve further study, because, as we show below (see Section 6.3 and Fig. 24), the sign of the trend is not what one might naively have expected.

6 BULGES AND DISCS

One of the virtues of our SerExp decompositions is that it allows us to study the scaling laws of discs and bulges. Recall that the second components required to fit bulge-dominated galaxies may not be discs. In addition, although it makes sense to speak of the central component in a disc-dominated galaxy, PYMORPH does not distinguish between central bulges and bars of such galaxies. Therefore, in what follows we would like to contrast the *R–L* and R–M_* relations for early types with those for their bulges, and these relations for late types with those for their discs. That is, we focus on the change which results from adding a small second component to the dominant one, rather than on the properties of the secondary component. See Gadotti (2008, 2009) and references therein for a discussion of the bars and pseudo-bulges in the centres of discs.

The structural properties of bulges can be reliably estimated only if the effective radius of the bulge is larger than about 80 per cent of the point spread function (PSF), half width half maximum (HWHM) (Gadotti 2008, 2009). The SDSS PSF HWHM is about 0.7 arcsec, and corresponds to about 1.3 kpc at the median redshift of $z \sim 0.1$. On the basis of a near-by sample ($z \sim 0.05$), Gadotti identified that about half of the bulges are smaller than ∼1 kpc which is the resolution limit of our work at $z \sim 0.1$. This raises the question of how reliable the PYMORPH estimates are for (small) bulges, and if resolution effects will bias our results. Note that in this section

Downloaded from https://academic.oup.com/mnras/article/443/1/874/1471537 by guest on 08 December 2023

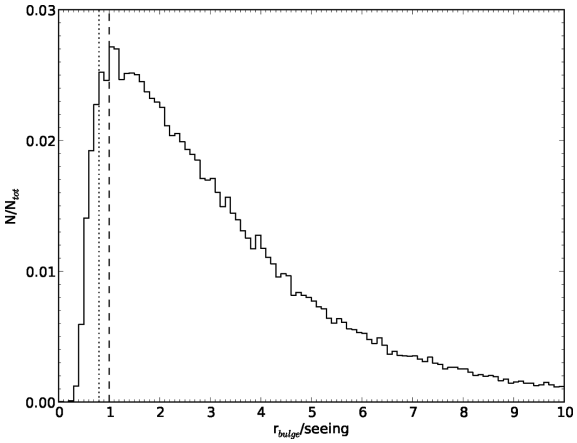

Figure 19. Distribution of the ratio between bulge effective radius and PSF half width half maximum (HWHM) for all galaxies in the sample (excluding bulgeless galaxies). The two vertical lines mark the positions where this ratio is 0.8 (dotted line) and 1 (dashed line). Only 7 per cent (11 per cent) of the bulges have effective radii below 0.8 (1) times the PSF HWHM. Had we used the semimajor axis rather than the circularized radius, these numbers drop to 3 and 7 per cent, indicating that our bulge decompositions should be reliable for the vast majority of our sample.

we are specifically studying the bulges of bulge-dominated systems while Gadotti analysed bulges for all galaxies with $M_* > 10^{10}$ $M_\odot$, therefore we expect our sample to be dominated by larger bulges.

The reliability of the PYMORPH bulges was partially addressed in Meert et al. (2013). But to allow a more direct comparison, Fig. 19 shows the distribution of bulge sizes in units of the PSF HWHM for galaxies in the early-type sample we study in this section, in a format which is similar to Gadotti's (2009) fig. 7. We find that a similar fraction of galaxies have bulges below the HWHM in our sample (11 versus 10 per cent for Gadotti) and about twice as many galaxies below the 80 per cent mark (7 versus 3 per cent for Gadotti). These numbers drop to 7 per cent (below the HWHM) and 3 per cent (below the 80 per cent mark) in our sample if we use the semimajor axis of the bulge rather than the circularized radius. Therefore, reliable estimates of bulge parameters should be possible for the vast majority of our sample. We have similar fractions to Gadotti, despite having a deeper sample, because we are specifically studying the bulges of bulge-dominated systems, and these tend to be the more massive galaxies with larger half-light radii. We will see below that the half-light radii we recover are typically larger than 1 kpc, with no particular feature to indicate problems at around 1 kpc. Nevertheless, we reexamined the results reported below without including the bulges smaller than the HWHM and found no difference in the results.

Fig. 20 shows a related test of PYMORPH systematics: SerExp fits to noisy SerExp images tend to return unbiased estimates of the discs in systems with $B/T < 0.5$, but in objects where $B/T > 0.5$, the estimated bulge luminosities and sizes are slightly too faint and small at the bright end, and a little too bright at the faint end. However, these are rather small effects, so that the following study of the R–L relations of discs and bulges is meaningful.

The top and bottom panels in Fig. 21 show the relevant R–L and R–M_* relations. As we cautioned before, the conversion from L to M_* depends on M_*/L, which in turn depends on stellar population modelling as well as on an assumption about how the IMF depends on galaxy mass. But here, there is another reason to be cautious: our M_* estimates assume that M_*/L for the individual components is the same as that for the total. Since we are looking at bulges of early types and discs of late types, this assumption, while crude, should not be wildly wrong (the same would not be true for, e.g. the bulges of late types). Nevertheless, one might imagine that, as a result, we slightly under (over)-estimate the mass in the bulge(disc) component.

6.1 Little or no correlation for discs at low masses

There are two striking features about late types and their discs. First, although the $R_{\rm disc}-L_{\rm disc}$ and $R_{\rm disc}-M_{*\rm disc}$ relations are very curved, they run parallel to the corresponding R–L and R–M_* relations for late types; $R_{\rm disc}$ tends to be 0.1 dex larger than $R_{\rm hl}$. That $R_{\rm disc} > R_{\rm hl}$ is not surprising, since we know that late-type galaxies host small bulges which will contribute to the light at small radii. But that this should have produced a constant offset is not obvious. We address this question shortly.

Secondly, at $\log_{10}M_*/{\rm M}_\odot < 10.5$, the flattening of the $R_{\rm disc}-M_{*\rm disc}$ relation with respect to the slope at large M_* is quite

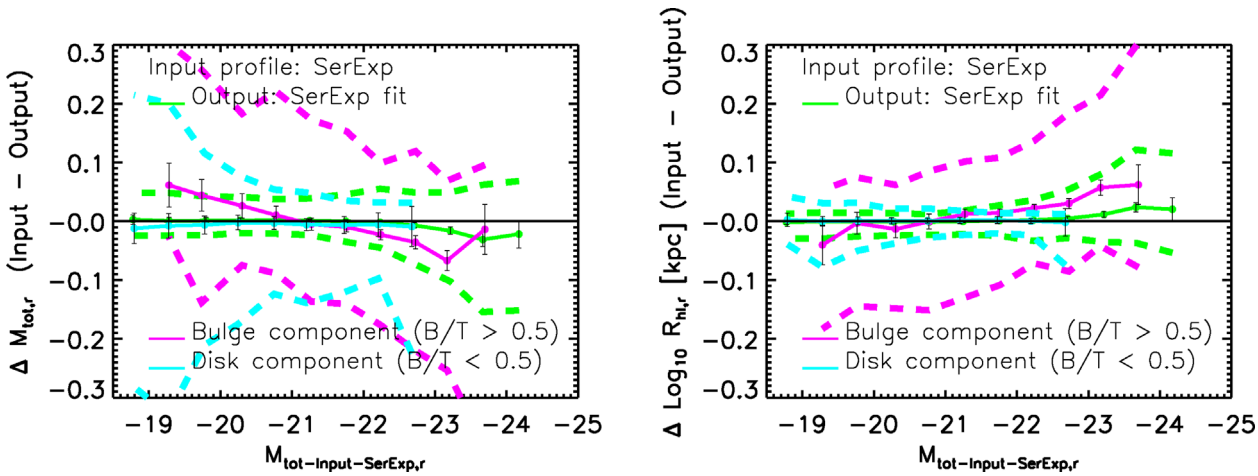

Figure 20. Biases in the estimated luminosities (left) and sizes (right) of the total (green), bulge (magenta) and disc (blue) components in SerExp fits to SerExp images (we restrict our analyses of the bulges and discs to those objects when they are the dominant component). The parameters of the total are usually unbiased, as are the discs of objects where $B/T < 0.5$. However, in objects where $B/T > 0.5$, the estimated bulge luminosities and sizes are slightly too faint and small at the bright end, and a little too bright at the faint end.

Downloaded from https://academic.oup.com/mnras/article/443/1/874/1471537 by guest on 08 December 2023

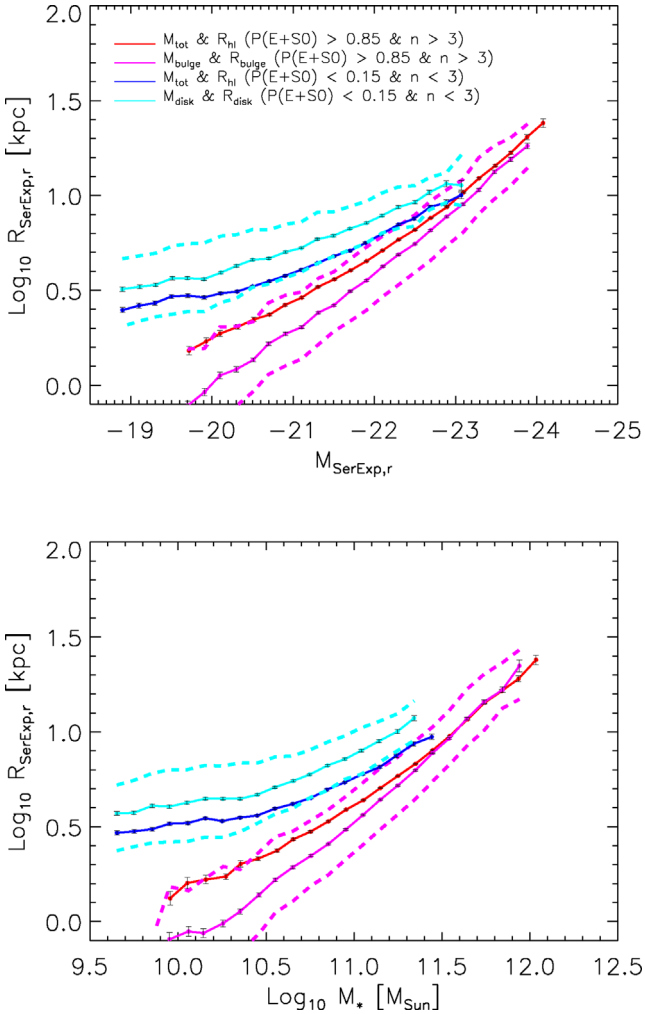

Figure 21. Similar to Fig. 13, but now contrasting the *R*–*L* (top) and *R*–M_* (bottom) relations for early types with those for their bulges, and these relations for late types with those for their discs. Note the severe flattening at $M < 3 \times 10^{10}\,\mathrm{M}_\odot$ in the relations for late types, and the absence of late types at the mass scales on which the bulge and total *R*–M_* relations become the same: $M > 2 \times 10^{11}\,\mathrm{M}_\odot$.

pronounced: there is almost no correlation between $R_{\rm disc}$ and $M_{\star\rm disc}$ at low masses. This flatness at the faint, low mass end is similar to that for Scds (see Figs 16 and 17 and related discussion): these discs are far from having constant surface brightness. Note that these sizes are significantly larger than the ∼1 kpc scale below which resolution effects might introduce a bias. Moreover, a flatter relation for discs is also seen in the lower panel in fig. 13 in Gadotti (2009).

6.2 A pure power law for bulges

The bulges are also interesting. In contrast to when the total light was used, there is almost no curvature in the relation for bulges which is well approximated by a single power law:

$$\langle R_{\rm bulge}|L_{\rm bulge}\rangle \propto L_{\rm bulge}^{0.85}. \quad (4)$$

The amplitude of the power law is such that the relation for bulges is approximately the same as for the total at very large luminosities; as *L* decreases, the *R*–*L* relation curves away from the $R_{\rm bulge}-L_{\rm bulge}$ relation, towards larger sizes. (There is a slight flattening of the relation at sizes smaller than about 1 kpc; these are the few objects for which the SDSS seeing may be becoming problematic.)

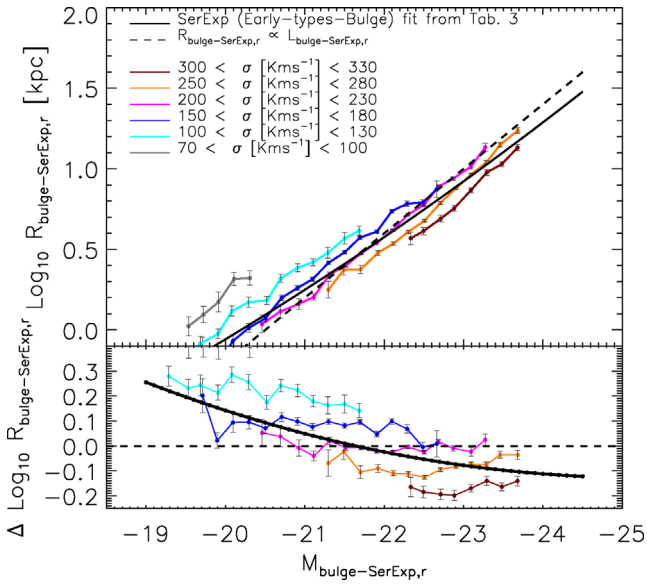

Figure 22. Same as Fig. 15, but showing $R_{\rm bulge}-L_{\rm bulge}$ for a number of bins in total velocity dispersion σ. Replacing $L_{\rm bulge}$ with M_* of the bulge yields the same result: the relation is a power law whose slope is 1 for all σ, but whose zero-point increases as σ decreases.

The power-law nature of the bulge relation suggests a picture in which the curvature in the early-type *R*–*L* relation arises as a consequence of adding a second component. However, there is an interesting puzzle: recall that Fig. 15 shows the *R*–*L* relation for a few narrow bins in velocity dispersion. This relation also has almost no curvature and, remarkably, it runs parallel to the $R_{\rm bulge}-L_{\rm bulge}$ relation (the *L* dependence of equation 4 is the same as of equation 3).

To explore this coincidence further, Fig. 22 shows the analogue of Fig. 15: the $R_{\rm bulge}-L_{\rm bulge}$ for fixed bins in σ. We find

$$\langle R_{\rm bulge}|L_{\rm bulge},\sigma\rangle \propto L_{\rm bulge}\,\sigma^{-1}. \quad (5)$$

Notice that the size is proportional to *L*. Replacing $L_{\rm bulge}$ with $M_{\star\rm bulge}$ makes no difference. That is, our SerExp bulges exhibit the scaling expected from the virial theorem, although the dependence on σ is different.

Finally, the bottom panel in Fig. 21 also shows that the $R_{\rm bulge}-M_{*\rm bulge}$ relation sits on top of that for early types at the largest masses, suggesting that the second component which contributes somewhat to the light contributes little to the mass. It is worth noting that this happens at the same mass scale, $M_* = 2 \times 10^{11}\,\mathrm{M}_\odot$, which Bernardi et al. (2011a) noted was significant for early types, and above which there appear to be no late-type galaxies (as is clear from this figure, as well as from Figs 12, 16 and 17).

In this context, it is worth noting that one gets approximately the same steep $R_{\rm bulge}-M_{*\rm bulge}$ relation if one combines the 'ellipticals' and 'classical bulges' shown in the upper panel in fig. 13 in Gadotti (2009). (The pseudo-bulges which are also shown in that panel are associated with small $B/T < 0.3$ values, so they would not be included in our sample of bulge-dominated systems.) While this is reassuring, Gadotti argues that it may better to think of the two populations as being physically distinct. This may be related to our finding of a small but systematic offset between the relations for ellipticals and S0s (Fig. 18). In addition, our Fig. 21 shows that

Downloaded from https://academic.oup.com/mnras/article/443/1/874/1471537 by guest on 08 December 2023

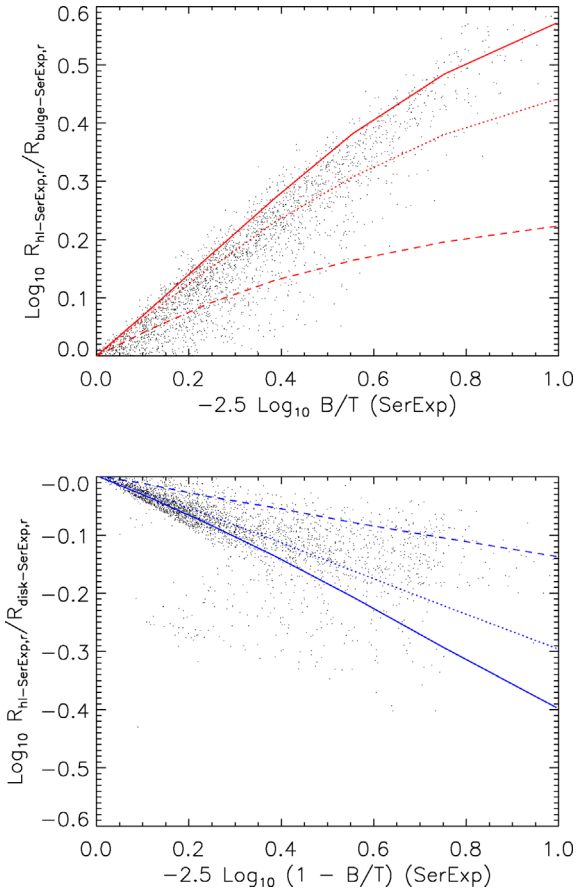

Figure 23. Correlation between $R_{\rm hl}/R_{\rm bulge}$ and B/T for early types (top panel) and between $R_{\rm hl}/R_{\rm disc}$ and B/T for late types (bottom panel). Although only objects with $-21.5 > M_r > -22.5$ are shown, we see qualitatively similar behaviour at other luminosities. The dashed, dotted and solid curves show the expected scaling for $n = 4$ bulges with exponential discs having $R_{\rm disc}/R_{\rm bulge} = 2$, 4 and 6.

the scatter around the mean bulge relation increases at smaller M_*, perhaps indicating that we are indeed combining two populations. On the other hand, at small M_* the sizes are increasingly prone to being biased by the seeing, so this may also be contributing to the increase in scatter.

6.3 The smallness of bulges

Why are the *R–L* relations for the discs and bulges so different from those for the total light?

To address this, we selected a subset of the early-type sample with $-21.5 > M_r > -22.5$. Fig. 23 shows that there is a strong correlation between $R_{\rm hl}/R_{\rm bulge}$ and B/T (at this fixed M_r) for the early-type sample. If the total is 0.55 mag brighter than the bulge ($B/T = 0.6$), then the half-light radius of the total is about 0.35 dex larger than that of the bulge. A similarly tight correlation is seen for other M_r. What causes this?

Suppose we start from the power law $R_{\rm bulge}$–$L_{\rm bulge}$ relation. $L_{\rm bulge}$, with a given value of B/T, specifies a total magnitude $M_{\rm bulge} + 2.5\log_{10}(B/T)$. If n of the bulge is known, and we assume that the second component has an exponential profile, then the half-light radius of the combined profile is fully specified only if we also know $R_{\rm disc}/R_{\rm bulge}$ (see Appendix B). (Recall that, although we use the word disc, we do not mean to imply that the second component is necessarily a disc.) The curves show the expected relations

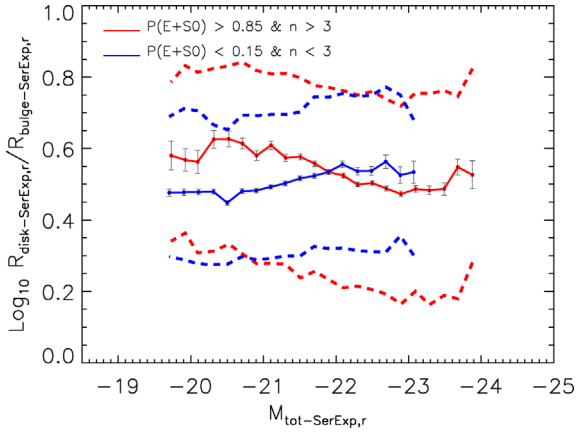

Figure 24. Dependence on total luminosity of the ratio of the size of the extended component to that of the bulge for early- (red, decreases slightly as luminosity increases) and late-type (blue, approximately independent of luminosity) galaxies. The dashed lines show the range which encompasses 86 per cent of the data.

between $R_h/R_{\rm bulge}$ and B/T for a de Vaucouleurs bulge with exponential disc for $R_{\rm disc}/R_{\rm bulge} = 2$, 4 and 6 (bottom to top). Although they are independent of the total luminosity (Appendix B shows why), the curves shift upwards slightly if $n > 4$ and downwards if $n < 4$.

Matching the data indicates that $R_{\rm disc}/R_{\rm bulge} \sim 5$ at $B/T < 0.7$ (if n is 5 rather than 4, then $R_{\rm disc}/R_{\rm bulge} \sim 4$), suggesting that the correlation is caused by the fact that PYMORPH uses second components with rather large scalelengths to account for the fact that a Sérsic bulge is not, by itself, always a good match.

Whether or not these large scalelengths are physically reasonable is an open question, but we show in Appendix B that these tend to be objects for which the single Sérsic fit returns large values of $n > 5$; these extended second components do appear to be necessary to provide a good fit. Indeed, fitting SerExp images with a single Sérsic profile requires large values of n if $0.4 < B/T < 0.7$ (bottom-left panel in Fig. 1).

The bottom panel in Fig. 23 shows a similar analysis of the late-type sample: $R_{\rm hl}/R_{\rm disc}$ as a function of $(1 - B/T)$. Most of the sample has $B/T < 0.2$ for which $\log_{10}(R_{\rm hl}/R_{\rm disc})$ differs from zero by -0.05 dex or less. Although this is in the opposite direction to the shifts for early types (as it should be), the resulting estimate of $R_{\rm disc}/R_{\rm bulge} \sim 4$ is similar. Of course, in this case, we expect $R_{\rm disc} \gg R_{\rm bulge}$, so the value of 4 does not require further explanation.

We can, of course, directly measure the ratio $R_{\rm disc}/R_{\rm bulge}$ for the objects in our early- and late-type samples. Fig. 24 shows that this ratio is indeed large, with only a weak dependence on L, and a somewhat larger scatter for early types. The actual median value, $\sim$3–4, is slightly smaller than the value we derived from the previous figure on the basis of the idealization that all galaxies were de Vaucouleurs bulges with exponential discs. Hence, we conclude that the differences between the relations shown in Fig. 21 can be traced to the fact that the bulge component in a galaxy tends to be substantially smaller than the second component.

Finally, recall from Fig. 18 that Es appear to be slightly larger than S0s of the same luminosity or mass. We remade Fig. 24 separately for Es and S0s; although we do not show this, the S0s lie slightly below the Es on this plot too. Thus, the small but significant trend shown in Fig. 18 results from the combined facts that the second component in Es is a larger multiple of the bulge size than it is in S0s, and Es (being more bulge dominated by definition) have larger

Downloaded from https://academic.oup.com/mnras/article/443/1/874/1471537 by guest on 08 December 2023

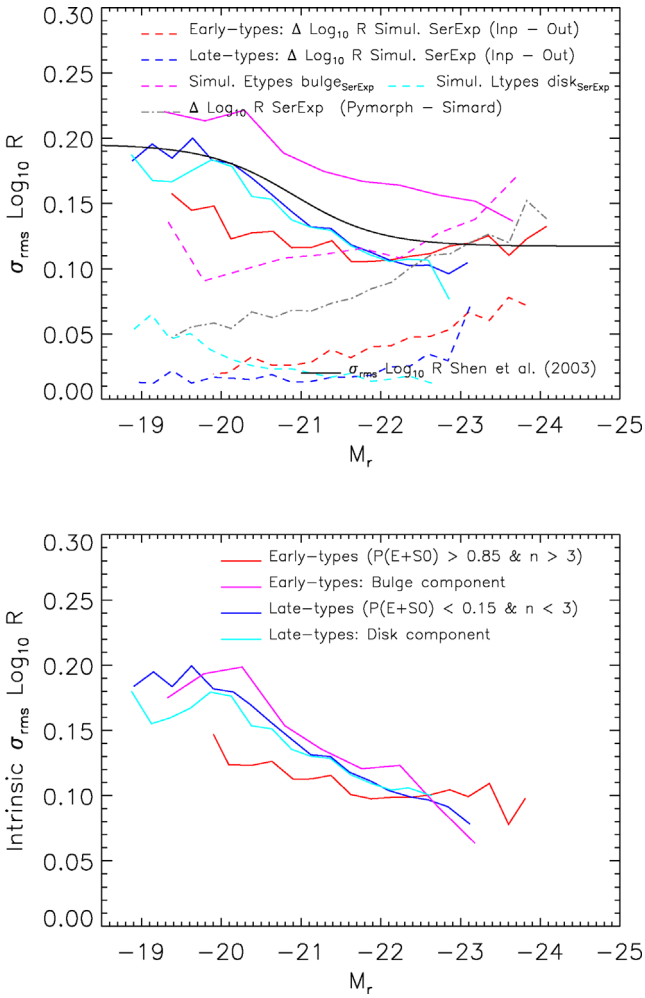

Figure 25. Observed (top) and intrinsic scatter (bottom) around various *R–L* relations as labelled (format similar to Fig. 14). In all cases, our upper limit to the intrinsic scatter decreases at large luminosities; this is particularly dramatic for later type galaxies.

bulges anyway. This strongly suggests that the second component in S0s and Es is not a disc, since, if anything, one expects S0s to have larger $R_{\rm disc}/R_{\rm bulge}$. While it is tempting to conclude that this second component may be intercluster light, as is almost certainly the case for cDs (Oemler 1976; Schombert 1986; Gonzalez et al. 2005) – the larger ratios at lower L perhaps indicating that this is more difficult to mask out for low L satellites in clusters – we do not have enough confidence in either our two-component decompositions or our BAC classifications to discuss 10 per cent effects. Nevertheless we do believe this is an interesting question particularly because Huertas-Company et al. report that the size difference is more dramatic at $z \sim 1$, and it is not obvious that the intercluster light hypothesis is even qualitatively consistent with this evolution.

6.4 Scatter

Before ending this section, Fig. 25 shows our estimate of the measured and intrinsic scatter around the mean *R–L* relations defined by bulges and discs, and compares them with corresponding estimates for early types and late types. Notice that the measured scatter is substantially smaller around the early-type relation than around any of the others. Since we argued earlier that the Shen et al. (2003) early-type sample is contaminated by later types, we believe this explains the difference between their results and ours in Fig. 14. Note also that the scatter around the relation for bulges is substantially larger than for the others.

Our estimates of the intrinsic scatter (shown in the bottom panel) come from subtracting, in quadrature, the measurement errors seen in simulations (dashed lines) from the total scatter measured in the data (corresponding solid lines), following the method described in Section 4.3. For this reason, we are almost certainly overestimating the intrinsic scatter. Nevertheless, it is interesting that for late-types discs and bulges, our estimates indicate that the intrinsic scatter decreases at large luminosities. For early types this decrease is less dramatic, with the scatter perhaps even levelling out at large luminosities. We believe these differences, along with the power-law nature of the bulge *R–L* relation, will prove to be useful for improving our understanding of how massive galaxies assembled their mass (e.g. Shankar & Bernardi 2009; Shankar et al. 2010).

7 SUMMARY

We used our automated image decomposition algorithm PYMORPH to study the effects of systematics in the size–luminosity relation of galaxies in the SDSS main sample (i.e. at $z \sim 0.1$) which arise from fitting different models to the images. We argued that when fitting to a SerExp profile, PYMORPH returns more physically reasonable results than does the algorithm of S11 (e.g. Figs A2 and A3 and related discussion).

We presented a novel diagnostic of whether or not the surface brightness profiles of galaxies are better thought of as having one or two components. The method works by fitting a number of single and two-component models to the image, and then studying the distribution in the n–B/T plane defined by the Sérsic index n associated with the single component fit and the ratio B/T of bulge to total light in the two-component fit. The way SDSS galaxies populate this plane suggests that they are not single component Sérsic systems. Rather, their distribution in n–B/T is more similar to that expected of two-component systems, with a Sérsic + exponential model faring somewhat better than the traditional de Vaucouleurs bulge with exponential disc model (Figs 1 and 3). That is, in bulge-dominated systems, allowing $n \neq 4$ provides a significantly improved fit. Indeed, we even find bulges with $n > 4$ in the SDSS (Fig. 2). Our conclusion that the SerExp model is preferred is consistent with a recent analysis of the the millennium galaxy catalogue (MGC), indicating that at least half of the galaxies at $z \sim 0.1$ are two-component SerExp systems (Allen et al. 2006).

Note that we do not conclude that, for relatively noisy data sets such as the SDSS, two-component models provide statistically better fits: e.g. Meert et al. (2013) have shown that for a large fraction of our DR7 sample, χ^2 per degree of freedom is not much better than it is for one-component fits. (For example, Fig. B3 shows an example of a galaxy for which the two fits are indistinguishable, but the estimated half-light radii are very different.) This is in agreement with S11 for the SDSS, and analyses of, e.g. the MGC by Allen et al. (2006), and the galaxy and mass assembly (GAMA) data set by Kelvin et al. (2012). Rather, the point is that the sizes and luminosities returned by the two-component SerExp model are less biased than those returned by fitting to a single Sérsic or de Vaucouleurs profile.

For objects brighter than L_*, the commonly adopted procedure – of fitting a single Sérsic profile to what is really a two-component SerExp system – leads to biases (Figs 6 and 7). The half-light radius is increasingly overestimated as n of the fitted single component increases; it is also overestimated around $B/T_{\rm SerExp} \sim 0.6$ (Fig. 8). For

Downloaded from https://academic.oup.com/mnras/article/443/1/874/1471537 by guest on 08 December 2023

such objects that are likely to be early type, but have a significant exponential component, the assumption of a single Sérsic component is particularly bad. However, the net effect on the size–luminosity relation is small, except for the most luminous tail (Fig. 11).

On the other hand, fitting a realistic model is necessary to obtain sensible estimates of the intrinsic scatter around the mean *R–L* relation. Having done this, we showed that the scatter in sizes correlates with velocity dispersion (Fig. 15), and the rms scatter decreases at large luminosity (Fig. 14), although for early types it may level off to a constant value of about 0.1 dex at large luminosities. This should provide tight constraints on the nature and number of mergers required to assemble the most massive galaxies.

We also studied how the *R–L* relation depends on galaxy morphology. Our Fig. 16 shows one of the first uses of Bayesian-classifier-based weights in the estimation of the *R–L* scaling relation for different morphologies (e.g. Aguerri et al. 2012). We found that, even if we allow for finer bins in morphology, there seem to be only two fundamental *R–L* relations, both of which are slightly but statistically significantly curved (Figs 13, 16 and 17 and Tables 3 and 4).

Of course, a closer inspection does reveal subtle dependences on morphology. Amongst early types, S0s tend to be about 0.06 dex smaller than Es of the same luminosity (Fig. 18). This difference is smaller than the ∼40 per cent reported by Huertas-Company et al. (2012) at $z \sim 1$. We argued that this subtle difference argues against interpreting the second component in SerExp fits as a disc. It is particularly interesting in view of the fact that the two types show very different trends as a function of age (Bernardi et al. 2010), so we expect that it, and its evolution, should yield interesting new constraints on models of how early-type galaxies assembled their stellar mass. Similarly, amongst late types, faint Sbs tend to be ∼0.1 dex smaller than Scds of the same luminosity, but these differences decrease as luminosity increases.

Our two-component fits allowed us to study the *R–L* relations for the bulges of early types and discs of late types. Although the *R–L* relations for the total light in early and late types are curved (Fig. 13), the relation defined by the bulges in bulge-dominated (typically early-type) galaxies is remarkably straight: $\langle R_{\rm bulge}|L_{\rm bulge}\rangle \propto L_{\rm bulge}^{0.85}$ (Fig. 21). The relation for discs of disc-dominated galaxies runs parallel to the *R–L* relation for late-type galaxies, being offset upwards by about 0.1 dex. For discs, this curvature is so pronounced that, at the faint, low mass end, there is almost no correlation between R and L or M_* (Figs 17 and 21). We argued that, both for early- and late-type galaxies, these differences arise because PYMORPH uses second components for which the half-light radius is ∼3−4 times larger than that of the central bulge (Figs 23, 24 and Appendix B). It is not clear if for early types this is physically reasonable – but extended second components are clearly necessary for the SerExp fits (Figs B2 and B3).

The two mass scales, $M_* \sim 3 \times 10^{10}\,{\rm M}_\odot$ and $M_* \sim 2 \times 10^{11}\,{\rm M}_\odot$, previously identified by Bernardi et al. (2011a,b), are clearly visible in our *R–L* relations (e.g. Fig. 12). For early types, the former, is, among other things, the mass scale at which galaxies are maximally dense. Below this scale the R–M_* relation curves upwards with respect to the power law which best describes the full range of M_* (Figs 11 and 16). Bernardi et al. suggest that this is because the disc component becomes more significant at these low masses. The larger mass scale ($M_* \sim 2 \times 10^{11}\,{\rm M}_\odot$) is where the *R–L* relation of early-type curves upwards with respect to the power law which best describes the full range of M_* (Fig. 12).

Whether or not these scales are associated with the onset of different physics is the subject of ongoing debate. For example, Graham & Worley (2008) have pointed out that curvature in the *R–L* relation may arise as a consequence of linear $n-L$ and central surface brightness–L relations; the linearity of these would not be suggestive of changing physics along the relation. Our single Sérsic-based fits do indeed yield pure power laws for these relations, at least for early types above $M_* = 3 \times 10^{10}\,{\rm M}_\odot$. But they are not pure power laws for our SerExp reductions, which we believe we have demonstrated are more appropriate.

Bernardi et al. attribute the change at $M_* \sim 2 \times 10^{11}\,{\rm M}_\odot$ to a change in the assembly histories – to ones in which major dry mergers become important. So it is interesting that it is at this mass scale that the bulge and total R–M_* relations become the same, despite being very different at smaller masses (Fig. 21). This is particularly remarkable in light of recent work showing that early types below this mass scale tend to be fast rotators (Cappellari et al. 2012). It may be that our SerExp bulge–disc decompositions of the images are reflecting this change in the kinematics. Although running PYMORPH on the images in other SDSS bands would allow us to determine colours and colour gradients of the individual components – perhaps providing further insight – this is beyond the scope of this work.

Our analysis indicates that these same two mass scales are also significant for late-type galaxies. At $M_* < 3 \times 10^{10}\,{\rm M}_\odot$, the $R-M_*$ relation for late types (and their discs) flattens significantly (Figs 16, 17 and 21); and $M_* = 2 \times 10^{11}\,{\rm M}_\odot$ marks the mass scale above which there are almost no late types (Figs 17 and 21).

Given the large differences between the relation for bulges and that for early types at smaller masses and luminosities (Fig. 21), it is remarkable that the slope of the *R–L* relation for bulges is essentially the same as that for early types within a fixed bin in velocity dispersion (Fig. 15). In fact, at fixed $L_{\rm bulge}$ and σ, the mean size scales as $R_{\rm bulge} \propto L_{\rm bulge}/\sigma$ (Fig. 22). Although the scaling proportional to $L_{\rm bulge}$ is consistent with the virial theorem (if $L_{\rm bulge} \propto M_{\rm bulge}$), the dependence on σ is not. Why this should be so is an open question.

Finally, we find that the scatter around the mean *R–L* relation decreases as L increases (and similarly for R–M_*), except for early types, where it may flatten at 0.1 dex (Fig. 25). We expect this to provide a useful probe of how massive galaxies assembled their mass (e.g. Shankar & Bernardi 2009; Shankar et al. 2010).

ACKNOWLEDGEMENTS

This work was supported in part by NASA grant ADP/NNX09AD02G and NSF/0908242. MB and RKS are grateful to the Meudon Observatory for its hospitality during 2011 and 2012 June. FS acknowledges support from a Marie Curie grant.

REFERENCES

Abazajian et al., 2009, ApJS, 182, 543
Aguerri J. A. L., Huertas-Company M., Sánchez Almeida J., Muñoz-Tuñón C., 2012, A&A, 540, 136
Allen P. D., Driver S. P., Graham A. W., Cameron E., Liske J., de Propris R., 2006, MNRAS, 371, 2
Bernardi M., 2009, MNRAS, 395, 1491
Bernardi M. et al., 2003a, AJ, 125, 1849
Bernardi M. et al., 2003b, AJ, 125, 1866
Bernardi M., Hyde J. B., Sheth R. K., Miller C. J., Nichol R. C., 2007, AJ, 133, 1741
Bernardi M., Shankar F., Hyde J. B., Mei S., Marulli F., Sheth R. K., 2010, MNRAS, 404, 2087
Bernardi M., Roche N., Shankar F., Sheth R. K., 2011a, MNRAS, 412, L6
Bernardi M., Roche N., Shankar F., Sheth R. K., 2011b, MNRAS, 412, 684

Downloaded from https://academic.oup.com/mnras/article/443/1/874/1471537 by guest on 08 December 2023

Binggeli B., Sandage A., Tarenghi M., 1984, AJ, 89, 64
Blanton M. R. et al., 2003, ApJ, 594, 186
Baldry I. K., Glazebrook K., Brinkmann J., Ivezić Z., Lupton R. H., Nichol R. C., Szalay A. S., 2004, ApJ, 600, 681
Bruce V. A. et al., 2012, MNRAS, MNRAS, 427, 1666
Cappellari M. et al., 2012, MNRAS, 432, 1862
Cimatti A. et al., 2008, A&A, 482, 21
Ciotti L., Bertin G., 1999, A&A, 352, 447
de Vaucouleurs G., 1948, Ann. Astrophys., 11, 247
Emsellem E. et al., 2011, MNRAS, 414, 888
Fukugita M. et al., 2007, AJ, 134, 579 (F07)
Gadotti D. A., 2008, MNRAS, 384, 420
Gadotti D. A., 2009, MNRAS, 393, 1531
Gonzalez A. H., Zabludoff A. I., Zaritsky D., 2005, ApJ, 618, 195
Graham A., 2013, in Oswalt T. D., Keel W. C., eds, Planets, Stars and Stellar Systems. Springer Science+Business Media Dordrecht, p. 91, preprint (arXiv:1108.0997)
Graham A. W., Worley C. C., 2008, MNRAS, 388, 1708
Graham A. W., Erwin P., Trujillo I., Asensio Ramos A., Worley C. C., 2003, AJ, 125, 2951
Huertas-Company M., Aguerri J. A. L, Bernardi M., Mei S., Sánchez Almeida J., 2011, A&A, 525, 157
Huertas-Company M. et al., 2012, MNRAS, 428, 1715
Hyde J. B., Bernardi M., 2009, MNRAS, 394, 1978
Johnston E. J., Aragón-Salamanca A., Merrifield M. R., Bedregal A. G., 2012, MNRAS, 422, 2590
Kelvin L. S. et al., 2012, MNRAS, 421, 1007
Meert A., Vikram V., Bernardi M., 2013, MNRAS, 433, 1344
Nair P., Abraham R. G., 2010, ApJS, 186, 427
Nair P., van den Bergh S., Abraham R. G., 2011, ApJ, 734, 1
Oemler A., Jr, 1976, ApJ, 209, 693
Saglia R. P. et al., 2010, A&A, 524, 6
Schombert J. M., 1986, ApJS, 60, 603
Sérsic J. L., 1968, Observatorio Astronómico. Córdoba
Shankar F., Bernardi M., 2009, MNRAS, 396, L76
Shankar F., Marulli F., Bernardi M., Dai X., Hyde J. B., Sheth R. K., 2010, MNRAS, 403, 117
Shankar F., Marulli F., Bernardi M., Mei S., Meert A., Vikram V., 2012, MNRAS, 428, 109
Shen S., Mo H. J., White S. D. M., Blanton M. R., Kauffmann G., Voges W., Brinkmann J., Csabai I., 2003, MNRAS, 343, 978
Sheth R. K., Bernardi M., 2012, MNRAS, 422, 1825
Simard L., Mendel J. T., Patton D. R., Ellison S. L., McConnachie A. W., 2011, ApJS, 196, 11 (S11)
Stoughton C. et al., 2002, AJ, 123, 485
Strateva I. et al., 2001, AJ, 122, 1861
Trujillo I. et al., 2006, MNRAS, 373, 36
van Dokkum P. G. et al., 2008, ApJ, 677, 5
Vikram V., Wadadekar Y., Kembhavi A. K., Vijayagovindan G. V., 2010, MNRAS, 409, 1379

APPENDIX A: SYSTEMATIC EFFECTS IN THE SIMARD ET AL. REDUCTIONS

The main text showed that the $R-L$ relation from single Sérsic fits using PYMORPH is in reasonably good agreement with that based on parameters from S11. However, Fig. A1 shows that, although the

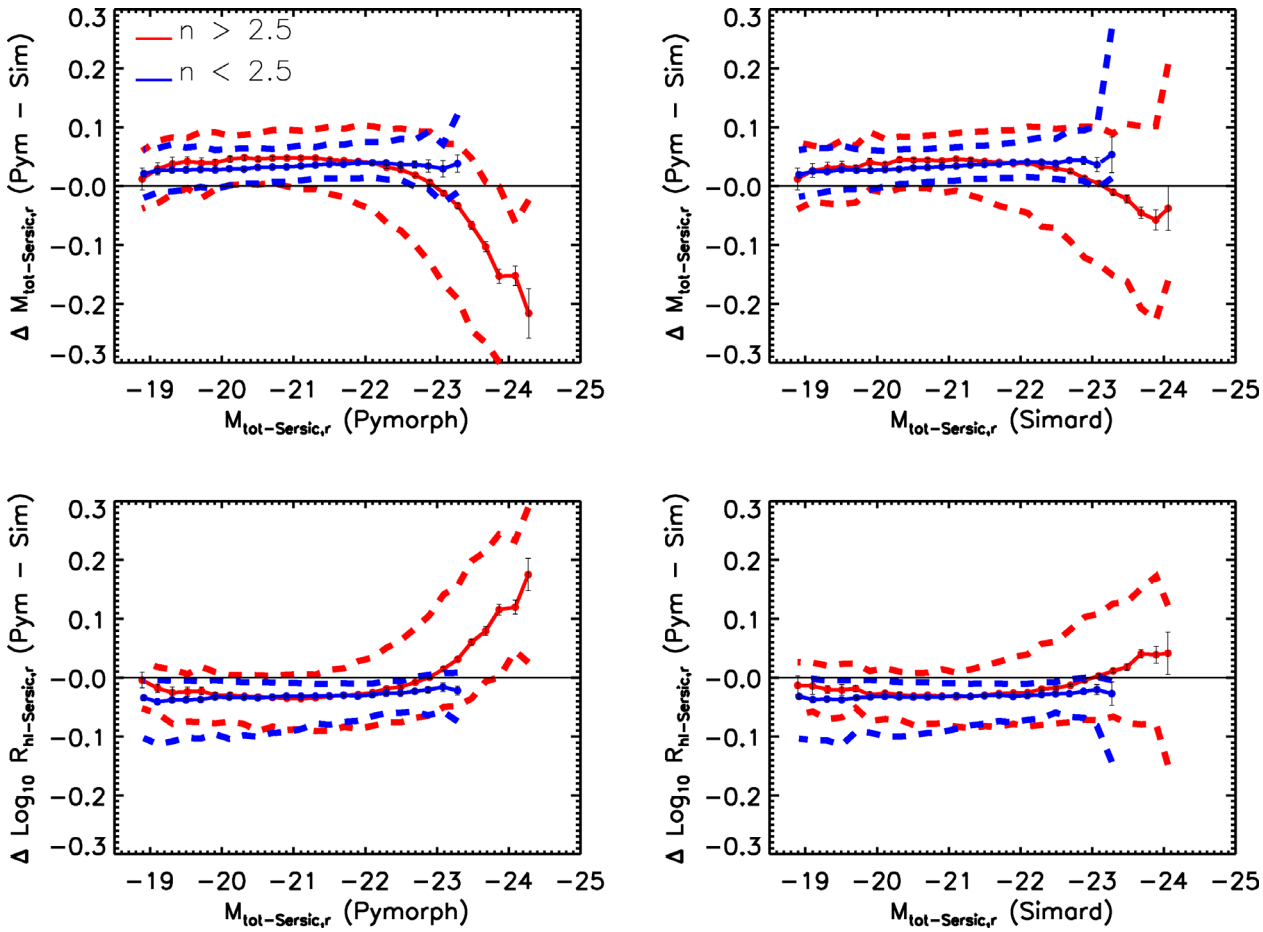

Figure A1. Differences between the S11 and PYMORPH reductions tend to be of the order of 0.04 mag fainter or 0.03 dex smaller in size, and approximately the same for all Sérsic indices, except for $M_r < -22.5$ where PYMORPH tends to be bigger and brighter if the Sérsic index $n > 2.5$ (i.e. if the galaxy is more likely to be early type). The solid lines and error bars show the median and the error on it; dashed lines show the range which encloses 86 per cent of the sample.

Downloaded from https://academic.oup.com/mnras/article/443/1/874/1471537 by guest on 08 December 2023

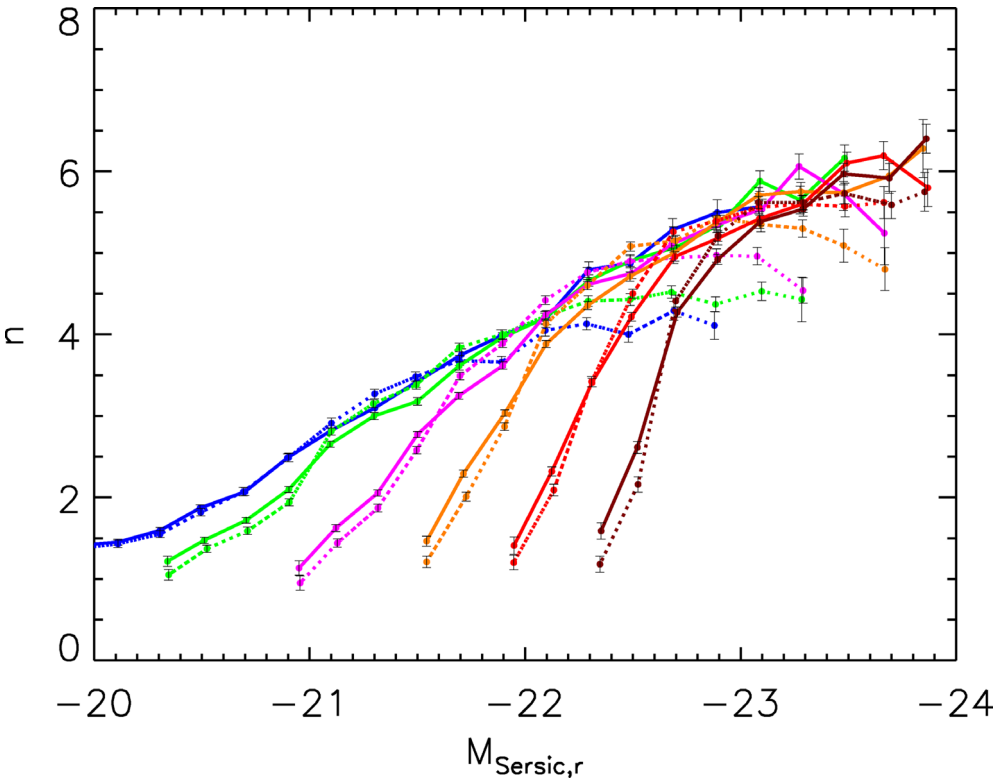

Figure A2. Our determination of the $n-L$ relation (symbols connected by solid lines) shows little or no redshift dependence (curves show results for adjacent redshift bins of width 0.02, starting from a bin centred on $z = 0.06$; the sample is magnitude limited so the lower L objects are missing from the higher-z bins). The sudden drop in n at the faint end of each redshift sample is due to the bimodal distribution in n at each L; it has nothing to do with evolution. Except for this, our determination shows little or no redshift dependence. In contrast, at high luminosities, the S11 reductions (dotted curves) lead to systematically smaller n as redshift decreases. We believe the implied evolution is unphysical, so conclude that the S11 reductions are systematically biased.

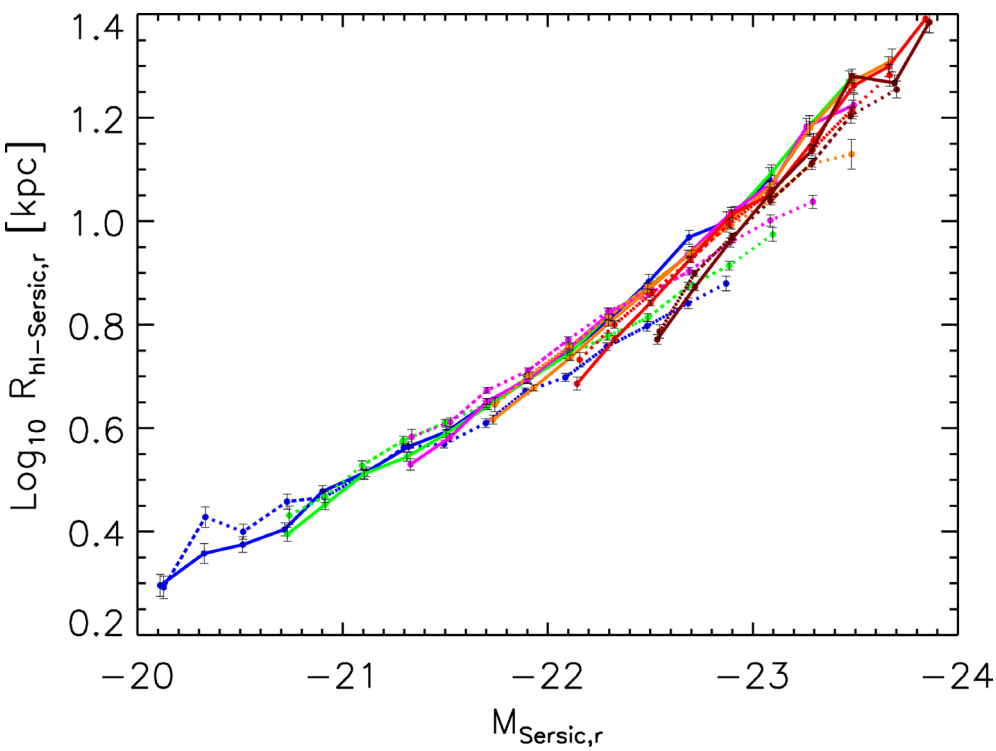

Figure A3. Similar to Fig. A2, but now for the $R-L$ relation: little or no redshift dependence is seen in our sample (symbols connected by solid lines); in contrast, at high luminosities, the S11 reductions (symbols connected by dashed lines) imply evolution towards smaller sizes as redshift decreases. We believe this implied evolution is unphysical, so conclude that the S11 reductions suffer from systematic biases.

Downloaded from https://academic.oup.com/mnras/article/443/1/874/1471537 by guest on 08 December 2023

two algorithms return similar sizes and luminosities for objects with $n < 2.5$ (PYMORPH is about 0.03 dex smaller and 0.03 mag fainter), the PYMORPH sizes and luminosities are systematically larger at large $M_{\rm tot}$. This bias for the biggest galaxies is particularly evident when shown as a function of $M_{\rm PyMorph}$.

Since the $R-L$ relation of the largest galaxies is particularly timely, we would like to determine which reductions are more reliable. Figs A2 and A3 show that the S11 reductions indicate substantial recent evolution towards smaller n and R at fixed L especially at larger L. We believe this evolution is unphysical, so conclude that the S11 reductions suffer from systematic biases. No such evolution is seen in the PYMORPH reductions, so we use them exclusively in the main text.

APPENDIX B: CORRELATION BETWEEN $R_{\rm BULGE}/R_H$ OR $R_{\rm DISC}/R_H$ AND B/T

Fig. 23 showed a correlation between the bulge (disc) to total size and B/T. This appendix shows why it arises.

The Sérsic profile is

$$I(r) = I_n \exp[-(r/r_n)^{1/n}] \tag{B1}$$

so the ratio of the light within r to the total light in the profile is

$$\frac{L_n(<r)}{L_n} = \frac{\int_0^{r/r_n} {\rm d}x\, x\, \exp(-x^{1/n})}{\int_0^{\infty} {\rm d}x\, x\, \exp(-x^{1/n})} = \gamma_{2n}\left[0, (r/r_n)^{1/n}\right], \tag{B2}$$

where γ_{2n} is the incomplete Gamma function. (For integer n, it can be written in terms of $\exp[-(r/r_n)^{1/n}]$ times a polynomial of degree $2n-1$ in $(r/r_n)^{1/n}$.)

Therefore, the half-light radius $r_{\rm h}$ of a SerExp profile satisfies

$$\frac{1}{2} = \frac{B}{T}\gamma_{2n}\left[0, \left(\frac{r_{\rm h}}{r_n}\right)^{1/n}\right] + \left(1-\frac{B}{T}\right)\gamma_2\left[0, \left(\frac{r_{\rm h}}{r_1}\right)^{1/n}\right]. \tag{B3}$$

For a given B/T, the right-hand side is a function of $r_{\rm h}/r_n$ and $r_{\rm h}/r_1 = (r_{\rm h}/r_n)(r_n/r_1)$, so it defines a different curve for each r_n/r_1, where $r_n = r_{\rm bulge}/(1.992n - 0.327)$ and $r_1 = r_{\rm disc}/1.67$. Note that the curves are independent of luminosity L; therefore L dependence only enters if the distribution of r_n/r_1 and/or B/T depend on L.

Fig. B1 shows $R_{\rm bulge}/R_{\rm hl}$ as a function of B/T for the early- (top) and late-type (bottom) samples defined in the main text for galaxies with $-21.5 > M_r > -22.5$; results are similar at other luminosities. The curves show the predicted relations (equation B3) for a de Vaucouleurs bulge ($n = 4$) with exponential disc. These depend on the ratio $R_{\rm disc}/R_{\rm bulge}$, for which we have chosen 2, 4 and 6. We argue in the main text that, despite the widespread use of the term 'bulge–disc' decomposition for two-component fits, for bulge-dominated galaxies, the 'disc' component is almost certainly not an inclined disc; rather, it is an extended second component which is required to fit the outer parts of the profile. But we call this second component 'disc' anyway.

The top panel shows a very strong correlation between $R_{\rm bulge}/R_{\rm hl}$ and B/T (at this fixed M_r) for the early-type sample. Clearly, if 20 per cent of the light is in a disc component, then the size is affected by at least this fraction. The well-known correlation between L and B/T, and the fact that early types span a large range of B/T, means that the bulge and early-type size–luminosity relations can be quite different. It is perhaps surprising that the half-light radius of the (second) disc component is typically more than 3–5 times larger than that of the bulge, particularly at $B/T < 0.7$. We argue in the main text that these large values of $R_{\rm d}/R_{\rm b}$ argue strongly against interpreting the more extended component as a flat exponential disc (not always viewed edge-on).

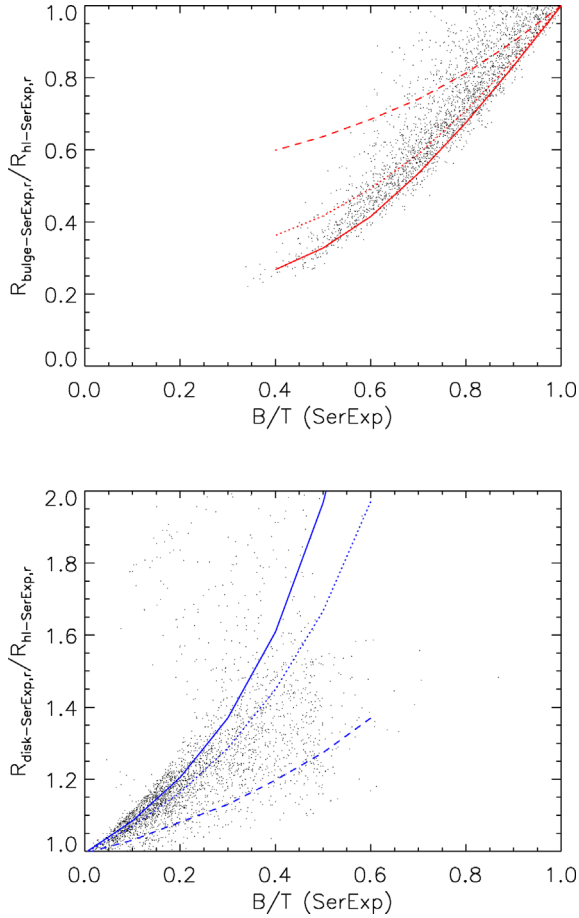

Figure B1. Correlation between $R_{\rm bulge}/R_{\rm hl}$ and B/T for early types (top panel) and between $R_{\rm disc}/R_{\rm hl}$ and B/T for late types (bottom panel). Although only objects with $-21.5 > M_r > -22.5$ are shown, we see qualitatively similar behaviour at other luminosities. Dashed, dotted and solid curves show the expected correlation for $n = 4$ bulges with $R_{\rm disc}/R_{\rm bulge} = 2$, 4 and 6.

The bottom panel shows $R_{\rm disc}/R_{\rm hl}$ and B/T for the late-type sample. Most of the sample has $B/T < 0.2$. Comparison with the smooth curves indicates that $R_{\rm disc}/R_{\rm bulge} \sim 5$ for most of the sample. In this case, we do expect the discs to be substantially larger than the bulges, so the results are sensible.

Fig. 23 in the main text shows this same information in a different format, which allows for a more direct understanding of the impact this correlation has on the relations shown in Fig. 21. And Fig. 24 in the main text shows that $R_{\rm disc}/R_{\rm bulge}$ is indeed ~3.

To address the question of large $R_{\rm d}/R_{\rm b}$ in our early-type sample, particularly at smaller B/T, Figs B2 and B3 show two examples. The format in both cases is the same: the top-left panel shows an ~20 arcsec field centred on the object, to get an idea of whether or not the object is in a crowded field. The top-right panel provides a closer look at the object. The panel just below it shows the best-fitting SerExp model, and the middle-left panel shows residuals from this fit. The bottom-left panel shows the one-dimensional surface brightness profile, and our Sérsic (solid magenta), deVExp (solid blue) and SerExp (solid red) fits; dotted and dashed curves show the corresponding disc and bulge components. Bottom-right

Downloaded from https://academic.oup.com/mnras/article/443/1/874/1471537 by guest on 08 December 2023

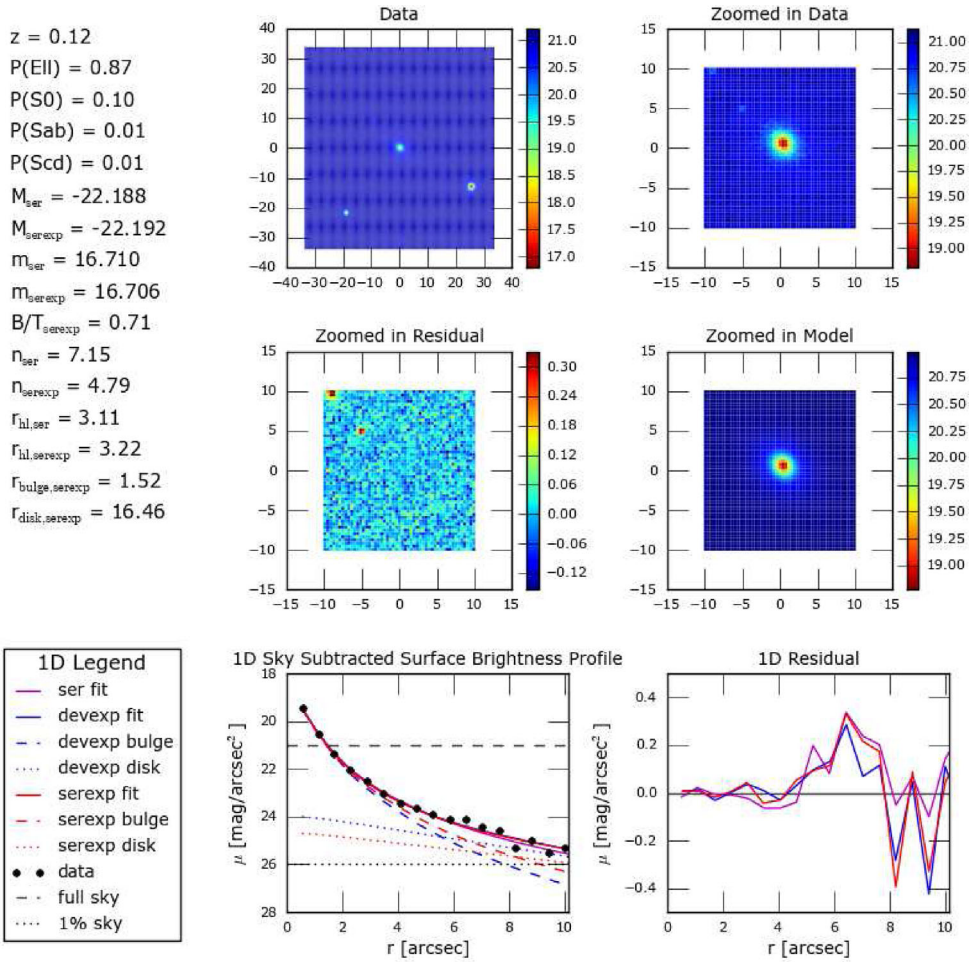

Figure B2. Example of an early-type galaxy with $M_r \sim -22$, large $R_\mathrm{d}/R_\mathrm{b} \sim 10$ and $B/T \sim 0.7$. Top-left panel shows a ∼20 arcsec field centred on the object; top-right panel provides a closer look. Middle-right panel shows the best-fitting SerExp model; middle-left panel shows residuals from this fit. Bottom-left panel shows the one-dimensional surface brightness profile (symbols), and our Sérsic (solid magenta), deVExp (solid blue) and SerExp (solid red) fits; dotted and dashed curves show the corresponding disc and bulge components. Bottom-right panel shows the associated residuals, indicating that all three models fit similarly well. Legend along the left shows the values of many quantities returned by the fits, and other information, such as the BAC p(type), for the object.

panel shows the associated residuals. The legend along the left shows the values of many quantities returned by the fits, and other information, such as the BAC p(type), for the object.

The object in Fig. B2, $B/T = 0.71$ and $R_\mathrm{d}/R_\mathrm{b} \sim 10$ is very likely to be an elliptical: $p(\mathrm{E}) = 0.87$. The Sérsic and SerExp fits return almost the same magnitudes ($M_r \sim -22.2$) and total half-light radii (∼3.15 arcsec). However, $n = 7.15$ for the single Sérsic fit, but $n = 4.79$ for the SerExp bulge. For the SerExp, as for the deVExp fits, the second component is clearly necessary. The $\chi^2_\mathrm{d.o.f.}$ values for these fits are similar.

In Fig. B3, the Sérsic magnitudes and half-light radii are slightly larger, but otherwise the qualitative trends are the same: the single Sérsic fit requires large n, and the second component in the SerExp fit clearly requires large $R_\mathrm{d}/R_\mathrm{b} \sim 6$.

Downloaded from https://academic.oup.com/mnras/article/443/1/874/1471537 by guest on 08 December 2023

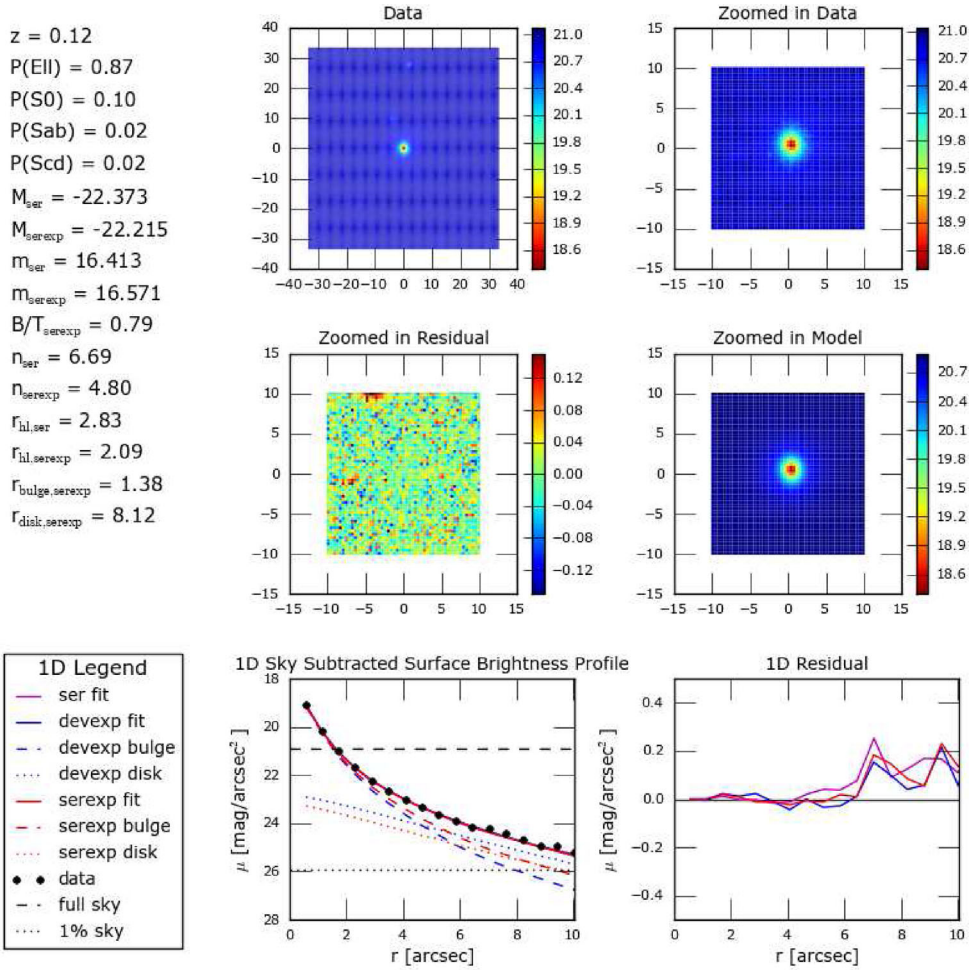

Figure B3. Same as previous figure, but for another early-type galaxy selected at random from among those with the same M_r and B/T range. Note again that our Sérsic, deVExp and SerExp fits all describe the one-dimensional surface brightness profile rather similarly. We argue in the text that this comes at the price of biased estimates of the total light and half-light radius, with the SerExp parameters being the least biased.

This paper has been typeset from a TEX/LATEX file prepared by the author.

Downloaded from https://academic.oup.com/mnras/article/443/1/874/1471537 by guest on 08 December 2023